

Nonlinear Dynamic Analysis of a Rotor-Porous Air Journal Bearing System With O-Rings Mounted

Kang Zhang

Hunan University State Key Laboratory of Advanced Design and Manufacturing for Vehicle Body

Kai Feng (✉ jkai.feng@gmail.com)

Hunan University State Key Laboratory of Advanced Design and Manufacturing for Vehicle Body

Wenjun Li

Hunan University State Key Laboratory of Advanced Design and Manufacturing for Vehicle Body

Lijun Song

Hunan University State Key Laboratory of Advanced Design and Manufacturing for Vehicle Body

Research Article

Keywords: Porous air journal bearings, O-rings mounted, Nonlinear dynamics, Theoretical and experimental analysis.

Posted Date: May 11th, 2021

DOI: <https://doi.org/10.21203/rs.3.rs-485873/v1>

License: © ⓘ This work is licensed under a Creative Commons Attribution 4.0 International License.

[Read Full License](#)

Version of Record: A version of this preprint was published at Nonlinear Dynamics on November 18th, 2021. See the published version at <https://doi.org/10.1007/s11071-021-07046-2>.

Nonlinear dynamic analysis of a rotor-porous air journal bearing system with O-rings mounted

Wenjun Li, Kang Zhang, Kai Feng*, Lijun Song

State Key Laboratory of Advanced Design and Manufacturing for Vehicle Body,
Hunan University, Changsha 410082, China

Corresponding Author: Kai Feng,

E-mail: jkai.feng@gmail.com

Abstract

Porous air journal bearings (PAJBs) with O-rings mounted are regarded as a potential choice to offer air levitation with a large load capacity and optimal start/stop characteristics, which are required in small-size and high-efficiency turbomachinery. However, the coupling of the mechanical properties of the O-rings and lubrication induce strong nonlinear characteristics, thereby affecting the dynamic responses of the rotor. In this study, a numerical model is presented, which is coupled with the excitation frequency-influenced stiffness and damping characteristics of O-rings, the Darcy's laws, air motion equations established by the air lubrication model, and the rotor and bearing motion equations. The model is well verified by the experimental results. The effect of the different system parameters on the performance of the rotor-PAJB system (RPS) is studied by analyzing the bifurcation diagrams, orbit, Poincaré maps, and FFT plots. Results show that the motion of the rotor is changed between periodic and quasi-periodic with the variation in rotational speed, external supply pressure, bearing clearance, and porous permeability. With O-rings mounted, the stability of RPS can be increased to hinder the rotor motion from changing from periodic to quasi-periodic. The effectiveness in increasing the stability of the RPS for the O-rings with SBR as the material is better than that with NBR but weaker than that with VMQ. Moreover, only a few number of O-rings have better effects on improving the stability of the RPS.

Keywords Porous air journal bearings · O-rings mounted · Nonlinear dynamics · Theoretical and experimental analysis.

Nomenclature

c	Bearing clearance (μm)
D	Bearing diameter (mm)
e_{ub}	Mass eccentricity of the rotor (mm)
F_x, F_y	Dimension film force in the x - and y -direction (N)
\bar{F}_x, \bar{F}_y	Dimensionless film force in the x - and y -direction
h_0	Nominal clearance (μm)
h, \bar{H}	Film thickness (μm) and dimensionless film thickness (h/h_0)
k	Permeability (mm^2)
L	Bearing length (mm)
m_b	Mass of the bearing (kg)
m_s	Half mass of the shaft (kg)
$\dot{m}_\theta, \dot{m}_r, \dot{m}_z$	Mass flow rates in the θ -, r -, and z -direction
p_a, p_s	Ambient and supply pressure (Pa)
p, P	Pressure (Pa) and dimensionless pressure (p/p_a)
r_0, r_s, r_r	Inner radius of the bearing, thickness of the porous material, radius of the rotor (m)
t, τ	Time and dimensionless time
k_b, b_b	Stiffness (MN/m) and damping ($\text{kN} \cdot \text{s/m}$) of O-rings
x_r, y_r, x_b, y_b	Rotor and bearing displacement in the x - and y -direction
r, θ, z	Coordinates in the r -, θ -, and z -direction
R, Z	Dimensionless coordinates in the r - and z -direction
X, Y	Coordinates in the vertical and horizontal directions
X_{rel}, Y_{rel}	Coordinates relative to the bearing in the vertical and horizontal

directions

ω	Angular speed of the rotor (rad/s)
ρ	Air density (kg/m ³)
μ	Air viscosity (Pa · s)
η	Porosity ratio of porous graphite

1 Introduction

Air bearings have the advantages of simple structure, high precision, and low friction [1]. Porous air journal bearings (PAJBs), which are a special type of aerostatic bearings, restrict the external pressured air by using the porous material to obtain a larger load capacity and better start/stop characteristics compared with the aerodynamic bearings [2]. Hence, PAJBs are broadly used in small-size and high-efficiency turbomachinery [3].

The first thought with regarding to the instability of PAJBs is air hammer because it belongs to the aerostatic bearings. Many studies [4-9] have been conducted to research the air hammer instability of PAJBs. These studies were mainly concerned about the influences of permeability and porosity, which are special parameters of the porous material. However, Refs [8, 9] found that the whirl instability is still a problem for PAJBs used under high rotational speed. Air hammer and whirl instability interrelate, and the whirl of the rotor may cause the air hammer. Jacob et al. [10] conducted a perturbation test to investigate the pneumatic stability of rotor-PAJB system (RPS). The frequencies of the whirl instability and the air hammer vibration were determined by using the bode plots and full spectral cascade plots, respectively. The data demonstrated that air hammer is a nonsynchronous excitation of the system resonant frequency. If the rotor-bearing natural frequency exceeds this self-sustaining frequency, then air hammer instability occurs. Thus, in addition to the air hammer, the stability of RPS must be examined, especially under the high rotational speed conditions.

Liu et al. [11] measured the dynamic response of a high rotational rotor supported on PAJBs and discussed the stability characteristics. The results showed that the bearing supply pressure and imbalance should be carefully checked when coupling with high rotational speed because they significantly influence the rotor synchronous and sub-synchronous motions. Wang et al. [12] investigated the nonlinear characteristics of a flexible rotor supported by two PAJBs. They found that varying the rotor speed and rotor mass has significantly influenced the system stability by analyzing the bifurcation of the rotor system. San Andrés et al. [13] and Wu et al. [14] analyzed the stability characteristics of the system with the rotor supported by porous air bearings. They used

tiling pad porous air bearings instead of PAJBs. This method can significantly increase the stability by changing the structural parameters of the bearings. However, the consistency of the porous pads cannot be easily ensured. Moreover, this design also adds to the complexity of the rotor-bearing system; accordingly, the system is difficult to adjust. These studies proved that the stability of the RPS must be enhanced.

Adding a flexible support element in the system is an efficient method to improve the stability of the air bearing rotor system at a high rotational speed. Adolfo and Ertas [15] adopted modular hermetically sealed squeeze film dampers to improve the system stability. Gu et al. [16] used a high-static low dynamic stiffness suspension to control the vibration of the rotating machine. Ertas [17] and Liu et al. [18] used metal mesh blocks to prevent system instability. Although these methods are novel, the new flexible support elements are either still in the concept stage or are structurally complicated. Besides these methods, using O-rings to support the bearings is a common method of offering a flexible support element in the system with the advantages of low cost and high compaction [19].

Many researchers studied the stability characteristics of the rotor-bearing system with O-rings mounted. Miyanaga et al. [20] performed the linear perturbation and the nonlinear transient methods to analyze the effect of support stiffness and damping of O-rings on the stability characteristics of herringbone-grooved aerodynamic journal bearings. Shabaneh et al. [21] analyzed the nonlinear dynamic characteristics of the rotor-bearing system with O-rings mounted. Dult [22] presented the development of preliminary equations by using differential operator algebra to analyze the motion of a simple viscoelastic rotor-shaft-system. Dousti et al. [23] addressed the nonlinear dynamic behavior of O-ring seals as the centering spring in the squeeze film dampers, and the model was incorporated in a linear and time transient rotor dynamic analyzer of a vertical turbocharger. Waumans et al. [24] used elastomeric O-rings in combination with a tunable squeeze film damper as the elastomer suspension in the experimental test to solve the dynamic stability problem of high-speed air bearings.

The above studies proved that O-rings have a significant influence on the stability of rotor-bearing systems. However, these studies traditionally considered the effect of O-

rings by simply presetting several groups of stiffness and damping values. This method is unreasonable. The relationship of the stiffness and damping of the O-rings depends on the material [25, 26] and frequency [27, 28], which means that the mechanical property of the O-rings is nonlinear.

Based on the above strength of the O-rings, the application of PAJBs with O-rings mounted will be a simple and effective way to achieve a high-speed and stable operation of the rotor in turbomachinery, and related studies are necessary. To date, few studies on the stability of RPS with O-rings mounted have been employed. The nonlinear characteristics of the RPS with O-rings mounted must be systematically studied because the mechanical properties of the O-rings and air are nonlinear.

In this work, a numerical model is established to investigate the nonlinear dynamic behaviors of RPS with O-rings mounted. The stiffness and damping characteristics of the O-rings are expressed on the basis of the Voigt model [29] with consideration of the influence of excitation frequency. Darcy's laws and air motion equation are coupled to establish an air lubrication model for the PAJBs. Two experimental test-rigs are designed and built to verify the numerical model. The dynamic characteristics of the RPS are tested on the basis of the rotor dynamic test-rig. The stiffness and damping characteristics of the O-rings used in the experiment are obtained in the excitation test-rig. The numerical results of the rotor dynamic characteristics of the RPS are first obtained by coupling the experimental tested stiffness and damping of the O-rings. Then, the numerical and experimental results of the rotor dynamic characteristics are compared to verify the numerical model. Finally, the rotor orbit, FFT, Poincaré maps, and bifurcation diagrams are adopted to systematically analyze the stability of the RPS in various parameters, including the materials and number of O-rings, rotational speed of the rotor, air supply pressure, nominal clearance, and permeability of the porous material.

2 Theory

2.1 Operating principle of the RPS with O-rings mounted

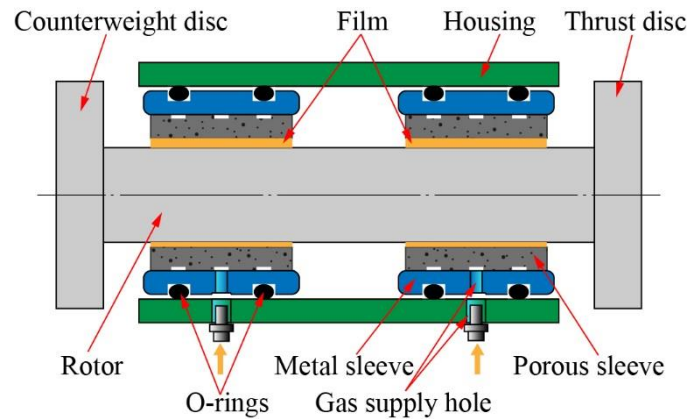


Figure 1 Schematic of the RPS with O-rings mounted

Figure 1 shows the RPS with O-rings mounted. The PAJB is constructed by coaxially and tightly fitted porous and metal sleeves. The porous sleeve is obtained by using the porous material. The porous sleeve is a special restrictor that has dense holes in the inner and surface of the material to restrict the external high-pressured air for ensuring that the bearing clearance can obtain a uniform distributed lubrication air film. This characteristic is called the aerostatic effect. Several grooves are made on the outer surface of the porous sleeve to ensure the air supply efficiency. The metal sleeve is obtained by using the metal and intersected by a hole. Two bearings are inserted into a housing, and the housing is fixed on the base. The O-rings are mounted between the metal sleeve and housing to support PAJBs, and they are supported by the housing. The holes are also designed to intersect the housing and coaxial with the hole of metal sleeve for allowing the external high-pressured air to enter the porous sleeve. The rotor structure of the turbomachinery is approximated as a rigid rotor with two discs at each end. One disc is designed with a mass equal to those of a turbine and a thrust runner. The other disc is designed at the opposite of the rotor to offer counterweight to balance the rotor mass. Accordingly, the weight of the rotor is shared on a 50–50 basis between two PAJBs.

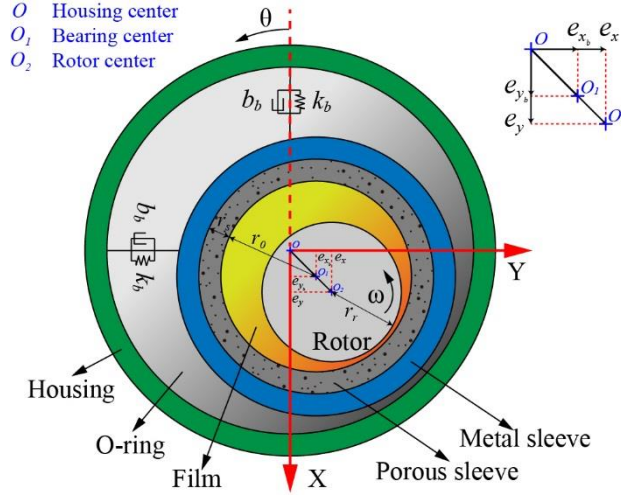


Figure 2 Geometric model of a PAJB

The housing geometric center is defined as the origin of the coordinate. The position of the bearing geometric center relative to the housing center will be changed with the various operating conditions because the PAJB is mounted by the O-rings, which are elastic. Then, the geometric model of the PAJB with O-rings mounted is presented in Figure 2. The inner radius of the bearing is r_0 , the thickness of the porous sleeve is r_s , the radius of the rotor is r_r , and the clearance of the bearing is defined as $c=r_0-r_r$.

The O-ring is simplified as the two pairs, which are located in the x - and y -direction, of stiffness and damping to support the bearing. The rotor is quickly rotated in the clockwise direction at the angular velocity ω , resulting in the aerodynamic effect of the air in the clearance. Accordingly, the rotor is finally levitated by the air film pressure determined by the coupling of the aerostatic and aerodynamic effects. The eccentricity ratios of the rotor and bearing relative to the center of housing are defined as $(\epsilon_{x_r}, \epsilon_{y_r})$ and $(\epsilon_{x_b}, \epsilon_{y_b})$, respectively. Then, the film thickness in a dimensionless form can be obtained:

$$\bar{H} = 1 + (\epsilon_{x_r} \cos \theta + \epsilon_{y_r} \sin \theta) - (\epsilon_{x_b} \cos \theta + \epsilon_{y_b} \sin \theta). \quad (1)$$

The dimensionless parameters are defined as follows:

$$h = c\bar{H}, \quad x_r = c\epsilon_{x_r}, \quad y_r = c\epsilon_{y_r}, \quad x_b = c\epsilon_{x_b}, \quad y_b = c\epsilon_{y_b}. \quad (2)$$

where (x_r, y_r) and (x_b, y_b) are the displacements of the rotor and bearing relative to

the center of the housing, respectively, which are also called the absolute displacements. The displacement of the rotor relative to the center of bearing, which is also called relative displacement, in the x - and y -direction can be expressed as follows:

$$\begin{pmatrix} x_{rel} \\ y_{rel} \end{pmatrix} = \begin{pmatrix} x_r \\ y_r \end{pmatrix} - \begin{pmatrix} x_b \\ y_b \end{pmatrix}. \quad (3)$$

2.2 Lubrication model

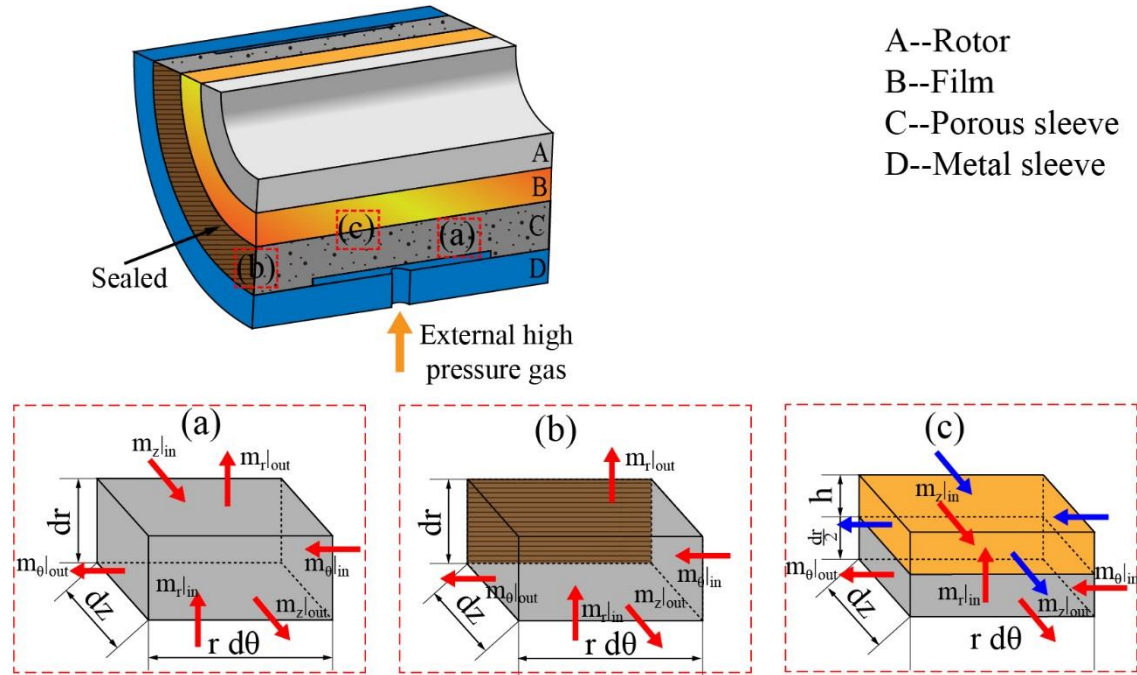


Figure 3 Airflow model in a PAJB

Figure 3 shows the airflow model in the PAJBs. The airflow region is meshed by small control volumes. The small control volumes of the overall solution domain are classified into three types with consideration of the characteristics of the structure and boundary. Different types of small control volumes have the same size in the bearing length direction and the same angle in the circular direction. The size of the small control volume is different in the radial direction for the porous and air film regions. The air flowing in and out the small control volume along three coordinate directions must satisfy the conservation of the mass flow rate, and it is expressed under the isothermal condition as follows:

$$\dot{m}_\theta|_{in} - \dot{m}_\theta|_{out} + \dot{m}_r|_{in} - \dot{m}_r|_{out} + \dot{m}_z|_{in} - \dot{m}_z|_{out} - \Delta\dot{m}_t = 0. \quad (4)$$

where subscripts *in* and *out* represent the mass flow rate of the air flowing in and out

the small control volume, respectively; and $\Delta\dot{m}_i$ represents the mass flow rate variation in a small controlled volume per unite time.

Type (a) shown in Figure 3 represents the small control volume at the interior of the porous sleeve with a size in the radial direction defined as dr . The air flows in and out of the small control volume from six surfaces. Assuming that the porous sleeve has the same permeability in different directions, the mass flow rate of the air in the porous sleeve is expressed on the basis of Darcy's law as follows:

$$\begin{aligned}\dot{m}_\theta &= -\rho \frac{k}{\mu} \frac{\partial p}{r \partial \theta} dr dz \\ \dot{m}_r &= -\rho \frac{k}{\mu} \frac{\partial p}{\partial r} r d\theta dz . \\ \dot{m}_z &= -\rho \frac{k}{\mu} \frac{\partial p}{\partial z} r d\theta dr\end{aligned}\quad (5)$$

The dimensionless mass conservation for the air flowing in the porous can be expressed by substituting Eq. 5 into Eq. 4:

$$\begin{aligned}-dR dZ \left[\bar{P} \frac{\partial \bar{P}}{R \partial \theta} \right]_{in} + dR dZ \left[\bar{P} \frac{\partial \bar{P}}{R \partial \theta} \right]_{out} - \left(R + \frac{dR}{2} \right) d\theta dZ \left[\bar{P} \frac{\partial \bar{P}}{\partial R} \right]_{in} \\ + \left(R - \frac{dR}{2} \right) d\theta dZ \left[\bar{P} \frac{\partial \bar{P}}{\partial R} \right]_{out} - R d\theta dR \left[\bar{P} \frac{\partial \bar{P}}{\partial Z} \right]_{in} + R d\theta dR \left[\bar{P} \frac{\partial \bar{P}}{\partial Z} \right]_{out} . \\ = \gamma \frac{\partial \bar{P}}{\partial \tau} R d\theta dR dZ\end{aligned}\quad (6)$$

The dimensionless parameters are defined as follows:

$$p = p_a \bar{P}, r = r_0 R, z = r_0 Z, dr = r_0 dR, dz = r_0 dZ, \tau = \omega t, \gamma = \frac{\mu \eta \omega r_0^2}{p_a k} . \quad (7)$$

where ρ is the air density, μ is the air viscosity, p is the air pressure, k is the permeability of porous sleeve, and η is the porosity of the porous sleeve.

Given that both end surfaces of the porous are sealed, the small control volume for meshing the end surfaces of the porous sleeve only has five surfaces for air flowing in and out, which is represented as type (b) in Figure 3. The size in the radial direction is also defined as dr . Then, the dimensionless mass conservation of air at the sealed end surfaces of the porous layer is expressed as follows:

$$\begin{aligned}
& -dRdZ \left[\bar{P} \frac{\partial \bar{P}}{R \partial \theta} \right]_{in} + dRdZ \left[\bar{P} \frac{\partial \bar{P}}{R \partial \theta} \right]_{out} - \left(R + \frac{dR}{2} \right) d\theta dz \left[\bar{P} \frac{\partial \bar{P}}{\partial R} \right]_{in} + \\
& \left(R - \frac{dR}{2} \right) d\theta dz \left[\bar{P} \frac{\partial \bar{P}}{\partial R} \right]_{out} - \gamma \frac{\partial \bar{P}}{\partial \tau} R d\theta dR dZ \quad . \quad (8) \\
& = \begin{cases} R d\theta dR \left[\bar{P} \frac{\partial \bar{P}}{\partial Z} \right] & \text{for in along } z\text{-direction} \\ -R d\theta dR \left[\bar{P} \frac{\partial \bar{P}}{\partial Z} \right] & \text{for out along } z\text{-direction} \end{cases}
\end{aligned}$$

Subscripts *in* and *out* for the *z*-direction are omitted. However, the air flowing in and out the small control volume must be distinguished from the *z*-direction, which is indicated on the right side of Eq. 8.

Type (c) shown in Figure 3 represents that the small control volume is constructed by two layers, which are porous and air film layers in the below and upper respectively. The surface between these two layers is also the inner surface of the porous sleeve. The thicknesses for the below and upper layers are $dr/2$ and h , respectively. The air only flows in and out of the small control volume from five surfaces without including the upper surface because the upper surface of the air film layer is overlapped with the shaft surface. Meanwhile, the air in the below and upper layers is also exchanged in the radial direction across the overlapped surface of these two layers. The air flow in the bearing clearance is assumed to be laminar. The mass flow rates in the upper layer are obtained on the basis of the air motion equation and expressed in the θ -, r -, and z -direction as follows:

$$\begin{aligned}
m_{\theta} &= -\frac{h^3}{12\mu} \rho \frac{\partial p}{r_0 \partial \theta} dz + \frac{\omega r_0}{2} \rho h dz \\
m_r &= -\frac{h^3}{12\mu} \rho \frac{\partial p}{\partial z} r_0 d\theta \quad . \quad (9) \\
m_z &= 0
\end{aligned}$$

The pressure gradient in the air film thickness direction is neglected for the ultra-thin air film in the bearing clearance. Eq. (9) shows that the mass flow rate in the z -direction in the clearance is zero. The dimensionless mass conservation for the air in the small control volume of category (c) is presented as follows by substituting Eqs. 5 and 9 into Eq. 4:

$$\begin{aligned}
& -dZ \left[PH^3 \frac{\partial P}{\partial \theta} \right]_{in} + dZ \left[PH^3 \frac{\partial P}{\partial \theta} \right]_{out} + \Lambda dZ ([PH]_{in} - [PH]_{out}) - \\
& \Gamma \frac{dRdZ}{2} \left[P \frac{\partial P}{\partial \theta} \right]_{in} + \Gamma \frac{dRdZ}{2} \left[P \frac{\partial P}{\partial \theta} \right]_{out} - d\theta \left[PH^3 \frac{\partial P}{\partial Z} \right]_{in} + \\
& d\theta \left[PH^3 \frac{\partial P}{\partial Z} \right]_{out} - \Gamma \frac{dRd\theta}{2} \left[P \frac{\partial P}{\partial Z} \right]_{in} + \Gamma \frac{dRd\theta}{2} \left[P \frac{\partial P}{\partial Z} \right]_{out} - \sigma \frac{\partial PH}{\partial \tau} d\theta dZ . \quad (10) \\
& = \begin{cases} \Gamma d\theta dZ \left[P \frac{\partial P}{\partial R} \right] & \text{for in along } r\text{-direction} \\ -\Gamma d\theta dZ \left[P \frac{\partial P}{\partial R} \right] & \text{for out along } r\text{-direction} \end{cases}
\end{aligned}$$

Subscripts *in* and *out* for the *r*-direction are also omitted. The air flowing in and out of the small control volume along the *r*-direction from the porous layer is distinguished by the right side of Eq. 10.

The external pressured air is supplied from the holes of the housing and metal sleeve to enter in the porous sleeve and gradually permeated into the clearance. The pressure value at the outer radial surface of the porous sleeve is equal to the external supply pressure as follows:

$$\bar{P} \Big|_{\bar{R}=1+\frac{r}{r_0}} = \bar{P}_s . \quad (11)$$

The air pressure in the air film and porous layers satisfies the continuity condition in the circular direction as follows:

$$\bar{P} \Big|_{\theta=0} = \bar{P} \Big|_{\theta=2\pi} . \quad (12)$$

At the end of the bearings, the air pressure in the air film is equal to the atmosphere pressure, and it is expressed as follows:

$$\bar{P} \Big|_{\bar{Z}=\pm\frac{L}{r_0}, \bar{R}=1} = 1 . \quad (13)$$

The pressure in the air film is defined as \bar{P}_0 with the dimensionless form as follows for easy description:

$$\bar{P}_0 = \bar{P} \Big|_{\bar{R}=1} . \quad (14)$$

The pressure distribution in the air film and porous sleeve can be obtained by solving Eqs. (6), (8), and (10) with the given air film thickness by using the finite difference method and Newton's iterative method. The bearing forces along the *x*- and *y*-direction

are expressed by integrating the air film pressure over the inner surface of porous sleeve:

$$\begin{bmatrix} F_x \\ F_y \end{bmatrix} = p_a R^2 \begin{bmatrix} \bar{F}_x \\ \bar{F}_y \end{bmatrix} = -p_a R^2 \int_{-\frac{L}{2D}}^{\frac{L}{2D}} \int_0^{2\pi} (\bar{P}_0 - 1) \begin{bmatrix} \cos \theta \\ \sin \theta \end{bmatrix} d\theta dz, \quad (15)$$

where \bar{F}_x and \bar{F}_y are the dimensional film forces in the x - and y -direction, respectively.

2.3 Force and motion analysis of the RPS

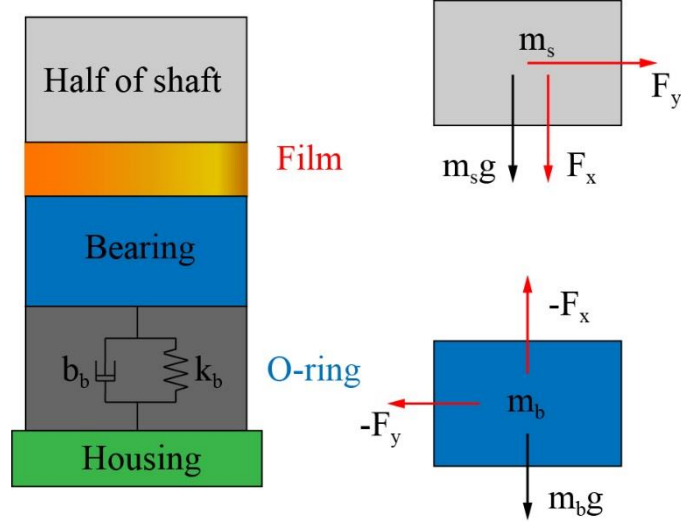


Figure 4 Mechanical model of the RPS

Figure 4 shows the mechanical model of the RPS. The half rotor with mass m_s is supported by the air film. The bearing with mass m_b is mounted by the O-rings that are also supported by the housing. The O-rings offer elastic force, and the stiffness and damping, denoted as k_b and b_b , respectively, can be obtained by the Voigt model [29] and expressed by empirical formulas as follows:

$$k_b = k' \exp(k'' f_v), \quad (16)$$

$$b_b = b' + \exp(-b'' f_v). \quad (17)$$

Eqs. (16) and (17) show that the stiffness and damping of the O-rings are frequency-dependent. The value of coefficients k' [Mn/m], k'' [1/kHz], b' [kN·s/m], and b'' [1/kHz] can be obtained by experimental test data. Meanwhile, f_v is the vibration frequency of the O-rings.

Ignoring the axial movement of the rotor, the transient motion of the rotor and bearing

relative to the center of housing in the x - and y -direction can be expressed as follows:

$$\begin{aligned}\ddot{x}_r &= (F_x + m_s e_{ub} \omega^2 \cos \omega t) / m_s + g \\ \ddot{y}_r &= (F_y + m_s e_{ub} \omega^2 \sin \omega t) / m_s\end{aligned}\quad (18)$$

$$\begin{aligned}\ddot{x}_b &= (-F_x - k_b \dot{x}_b - b_b x_b) / m_b + g \\ \ddot{y}_b &= (-F_y - k_b \dot{y}_b - b_b y_b) / m_b\end{aligned}\quad (19)$$

where (\ddot{x}_r, \ddot{y}_r) and (\ddot{x}_b, \ddot{y}_b) are the absolute accelerations of the rotor and bearing, respectively, in the x - and y -direction; (\dot{x}_b, \dot{y}_b) is the absolute velocity of the bearing in the x - and y -direction; m_r , m_b , and e_{ub} are the masses of the rotor and bearing and the unbalanced mass of the rotor; and g is the gravitational acceleration.

2.4 Numerical solution method

The absolute velocity of the rotor and bearing varying with time can be obtained as follows using Euler's method to integrate Eqs. (18) and (19):

$$\begin{aligned}\dot{x}_r(\tau) &= \dot{x}_r(\tau - \Delta\tau) + \ddot{x}_r(\tau)\Delta\tau \\ \dot{y}_r(\tau) &= \dot{y}_r(\tau - \Delta\tau) + \ddot{y}_r(\tau)\Delta\tau\end{aligned}\quad (20)$$

$$\begin{aligned}\dot{x}_b(\tau) &= \dot{x}_b(\tau - \Delta\tau) + \ddot{x}_b(\tau)\Delta\tau \\ \dot{y}_b(\tau) &= \dot{y}_b(\tau - \Delta\tau) + \ddot{y}_b(\tau)\Delta\tau\end{aligned}\quad (21)$$

where (\dot{x}_r, \dot{y}_r) denotes the absolute velocities of the rotor in the x - and y -direction; τ is the dimensionless time; and $\Delta\tau$ is the dimensionless time interval.

Then, the absolute displacements of the rotor and bearing can be finally obtained by integrating Eqs. (20) and (21) as follows:

$$\begin{aligned}x_r(\tau) &= x_r(\tau - \Delta\tau) + \dot{x}_r(\tau)\Delta\tau + \frac{1}{2}\ddot{x}_r(\tau)\Delta\tau^2 \\ y_r(\tau) &= y_r(\tau - \Delta\tau) + \dot{y}_r(\tau)\Delta\tau + \frac{1}{2}\ddot{y}_r(\tau)\Delta\tau^2\end{aligned}\quad (22)$$

$$\begin{aligned}x_b(\tau) &= x_b(\tau - \Delta\tau) + \dot{x}_b(\tau)\Delta\tau + \frac{1}{2}\ddot{x}_b(\tau)\Delta\tau^2 \\ y_b(\tau) &= y_b(\tau - \Delta\tau) + \dot{y}_b(\tau)\Delta\tau + \frac{1}{2}\ddot{y}_b(\tau)\Delta\tau^2\end{aligned}\quad (23)$$

The final characteristics of the RPS are obtained by iteration method, which is shown

in Figure 5. In the iteration at time τ , the absolute displacements of the rotor and bearing at time $\tau - \Delta\tau$ are substituted into Eq. (1) to obtain the air film thickness. The corresponding film pressure can be obtained by using Newton's iterative method to solve Eqs. (1), (6), (8), and (10) with an appropriate condition of convergence being set. The film forces are obtained by integrating the film pressure over the inner surface of the porous sleeve based on Eq. (15). Then, the film forces are substituted into Eqs. (18) and (19) to obtain the absolute acceleration of the rotor and bearing at time τ . According to Eqs. (20) and (21), the absolute velocity at time τ can be obtained by using the absolute velocity at time $\tau - \Delta\tau$ and absolute acceleration at time τ . Meanwhile, the absolute velocity and acceleration at time τ are used as variates of Eqs. (22) and (23) coupled with the absolute displacement at time $\tau - \Delta\tau$ to obtain the absolute displacement at time τ . Then, the absolute position, speed, acceleration of the rotor and bearing at time τ are used as the initial variates of the iteration at $\tau + \Delta\tau$. The characteristics of the RPS at time $\tau + \Delta\tau$ can be obtained by repeating the solution process at time τ . The results are output until the iteration steps reaching the preset.

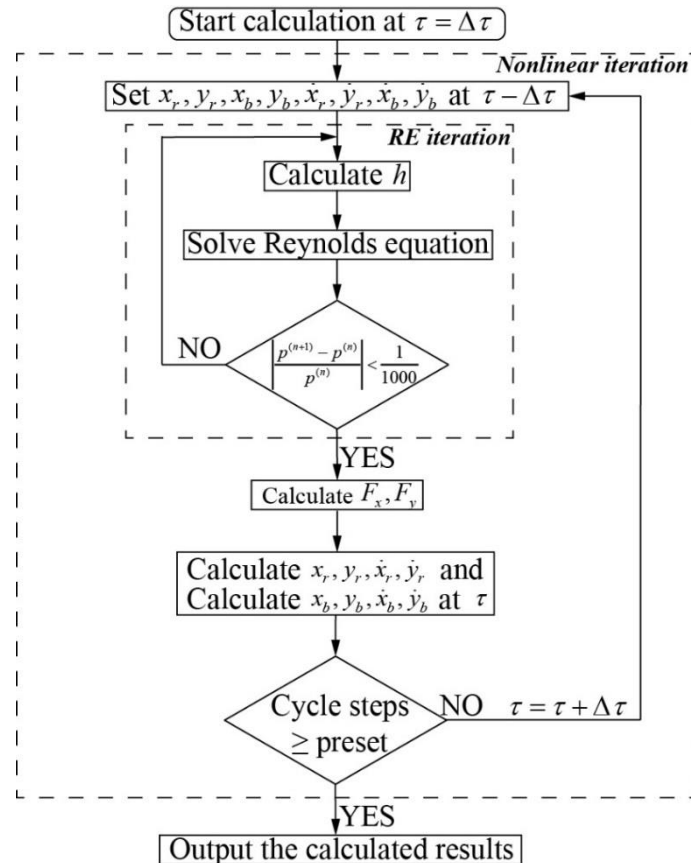


Figure 5 Flow chart of iteration method to obtain the characteristics of the RPS

3 Experimental verification

3.1 Experiment introduction

Two experiments are performed to verify the accuracy of the simulation program. The RPS experiment is carried out to obtain the dynamic motion characteristics of the rotor in different rotational speeds. The results are used to verify the validity of the numerical model and calculation process for obtaining rotor dynamic performance. The stiffness and damping characteristics of the O-rings, which are used in the RPS experiment, are obtained by excitation experiment. Meanwhile, the tested stiffness and damping of the O-rings are also used as the parameters in the numerical program to calculate the rotor dynamic performance.

3.2 Experiment of the RPS

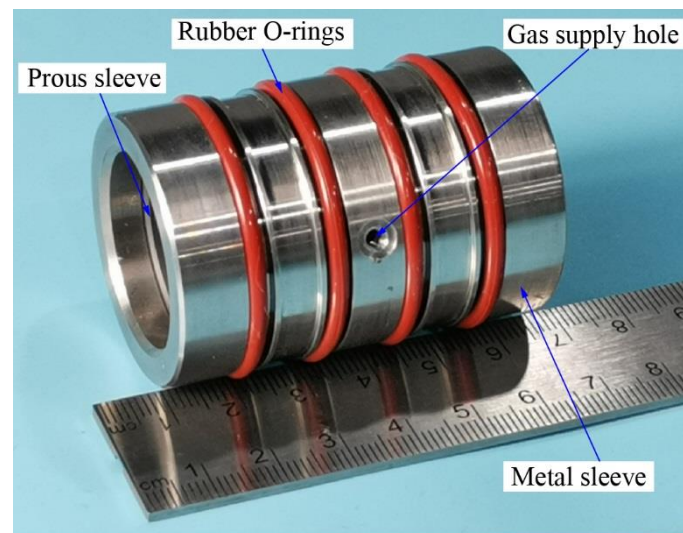


Figure 6 Photograph of the PAJB

Figure 6 shows the PAJB that is tested in the RPS experiment. The porous sleeve with graphite porosity as the material is coaxial with the metal sleeve that is made of 304 steel. The outer surface of the porous sleeve and the inner surface of the metal sleeve are locally glued with a superglue. Both end surfaces of the porous sleeve are sealed with a superglue. Several O-rings are mounted in the pre-designed grooves, which are on the outer surface of the metal sleeve. The O-rings must be able to fasten the metal sleeve with slight elastic force, which can offer effective stiffness to support the bearing and damping to absorb vibration. The material of the O-rings is hydrogenated nitrile

butadiene rubber (HNBR). An air supply hole is designed in the metal sleeve to allow the external high-pressured air to be supplied into the porous sleeve. Thus, the superglue must not drop into the supply hole of the metal sleeve and cover over the outer surface of the porous sleeve to ensure that high-pressured air is successfully and efficiently supplied into the porous sleeve.

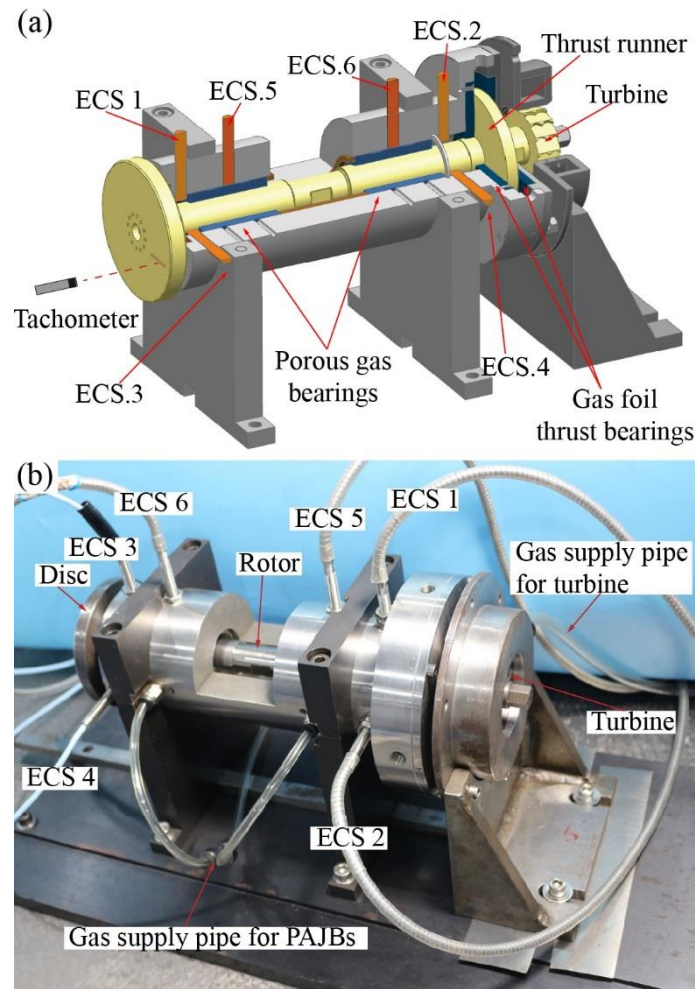


Figure 7 (a) Schematic diagram and **(b)** physical map of the rotor-bearing test-rig for RPS with O-rings mounted

Figures 7(a) and 7(b) show the schematic diagram and physical map of the rotor-bearing test-rig, respectively. A rotor is supported by two PAJBs. A double-pulse turbine and a thrust runner are designed at the same end of the rotor. Two foil thrust bearings are installed opposite to the two surfaces of the thrust runner to balance the axial forces. A counterweight disc is installed at the other end of the rotor to balance the weight of the rotor. Twelve circular uniform distributed holes that have the same diameter are

designed and manufactured in the counterweight disc. The unbalance mass of the rotor can be adjusted and changed by screwing the bolts in the holes. Two sets of eddy current sensors (ECSs. 1, 3 and 2, 4) are located at two ends of the rotor. Each set of ECSs must be simultaneously orthogonally installed along the x - and y -direction to obtain the vertical and horizontal vibration of the rotor. Moreover, ECSs 5 and 6 are installed at the top of the housing and aimed at the center position of PAJBs along the vertical direction to measure the movement of the bearings in the vertical direction. Meanwhile, a photoelectric tachometer is vertically aimed to the surface of counterweight disc to measure the rotational speed of the rotor. All test data from the sensors are recorded and used to analyze the dynamic characteristics of RPS.

To carry out the experiment, the high-pressured air is first supplied into the PAJBs to levitate the rotor. Accordingly, no friction exists between the PAJBs and rotor before the rotor rotated. Then, the high-pressure air from another air pipe, which is different from that of the PAJBs, is supplied along the radial direction of the turbine to drive the turbine. The turbine changes the energy of the high-pressured air to the kinetic energy of rotor. Lastly, the rotor is quickly initiated and rotated in high speed as it is levitated by the air film force.

Table 1 Parameters of the O-rings, PAJB, rotor and experiment environment

Object	Parameter	Value
O-ring	Material	HNBR
	Inside diameter	34.5 mm
	Section diameter	2.65 mm
	Compression ratio	15.1%
	Distribution number	4 in uniform
Bearing	Bearing mass, m_b	0.183 kg
	Bearing diameter, D	25 mm
	Bearing length, L	45 mm
	Porous thickness, r_s	2.5 mm
	Nominal clearance, h_0	15 μm
	Porous porosity ratio, η	0.1

	Porous permeability, k	$5.979 \times 10^{-9} \text{ mm}^2$
	Supply pressure, p_s	0.3–0.55 MPa
Rotor	Total mass, $2m_s$	2.057 kg
	Load	$2 \times 10.079 \text{ N}$
	Mass eccentricity of the rotor, e_{ub}	0.674 μm
	Rotational speed	0–30 krpm
Environment	Ambient pressure, p_a	0.1 MPa
	Air viscosity, μ	$19.8 \times 10^{-12} \text{ MPa} \cdot \text{s}$
	Temperature of the supplied air	294 K

Table 1 lists the detailed parameters of the O-ring, PAJBs, rotor, and environment for the experimental test. The total mass of the rotor is 2.057 kg, and the load is equally divided between two PAJBs. Hence, the supporting load of each PAJB is 10.079 N. The external pressured air with the pressure value varied between 0.3 MPa and 0.55 MPa is supplied into the PAJBs. The driving air of the turbine is supplied with the pressure changing from 0 MPa to 0.4 MPa to change the rotational speed of the rotor.

Figure 8 shows the tested waterfall plots (vertical direction) of the rotor and bearing centers relative to the center of housing for RPS with rotational speed changing from 12 krpm to 30 krpm. With regarding to the vibration characteristics of the rotor, the amplitude of the synchronous vibration is first increased and gradually decreased to be nearly unchanged with the increase in rotational speed. The comparison of the results between the external pressure values of 0.5 and 0.55 MPa indicates that the vibration characteristics of the rotor are nearly not changed. In terms of the vibration results of the bearings, the amplitude of the synchronous vibration is small and approximately equal to 1.5 μm . This value is nearly not changed with the variation in rotational speed and external supply pressure.

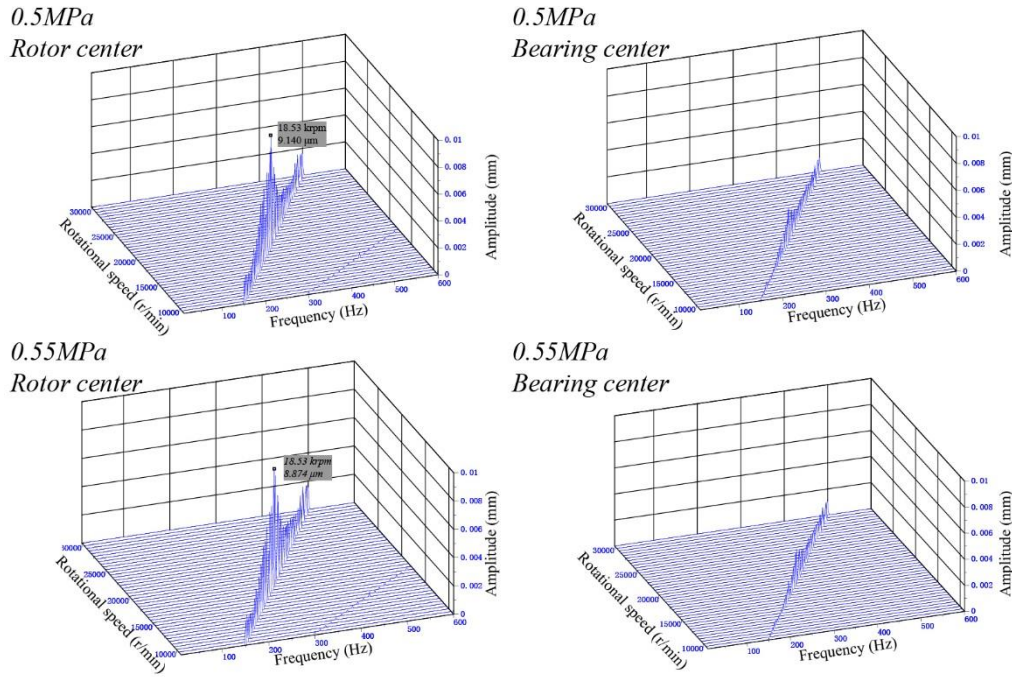


Figure 8 Waterfall plots (vertical direction) of the rotor and bearing centers for the RPS at the end of turbine

3.3 Excitation testing of the O-rings

Figure 9 shows the schematic diagram and physical map of the excitation test-rig. A new journal is designed with a special end. The structure and dimension parameter of the end are the same as those of the outer surface of the metal sleeve, which is presented in Figure 6. The new journal is fixed by the two clamping supports. A new sleeve is designed with its inner diameter being the same as that of the housing, which is presented in Figure 7. The new sleeve and O-rings construct the simple mechanical spring-mass damped system.

The new sleeve is excited by the electromagnetic exciter in the horizontal direction. Figure 8 shows that the vibration amplitude of the bearing is approximately $1.5 \mu\text{m}$. The vibration amplitude of the exciter may be set at $1.5 \mu\text{m}$ when exciting the new sleeve. The influence of the gravity of the new sleeve in the vertical direction can be ignored because the vibration amplitude is small. The characteristics of the vibration in the horizontal direction are also tested with the sensors. The experimental data of the vibration characteristics can be processed according to the research experiences of Luis

and Kim [30] to obtain the stiffness and damping of the O-rings at different frequencies. The stiffness and damping of a HNBR O-ring in 200–500 Hz frequency are shown in Figure 10. The stiffness is increased with the increase in excitation frequency, and the damping is decreased. The characteristics of the stiffness and damping varying with the frequency are fitted into Eqs. (16) and (17). The values of the coefficients k' , k'' , b' and b'' are 0.8502, 1.46, 0.0121 and -3.9257 respectively.

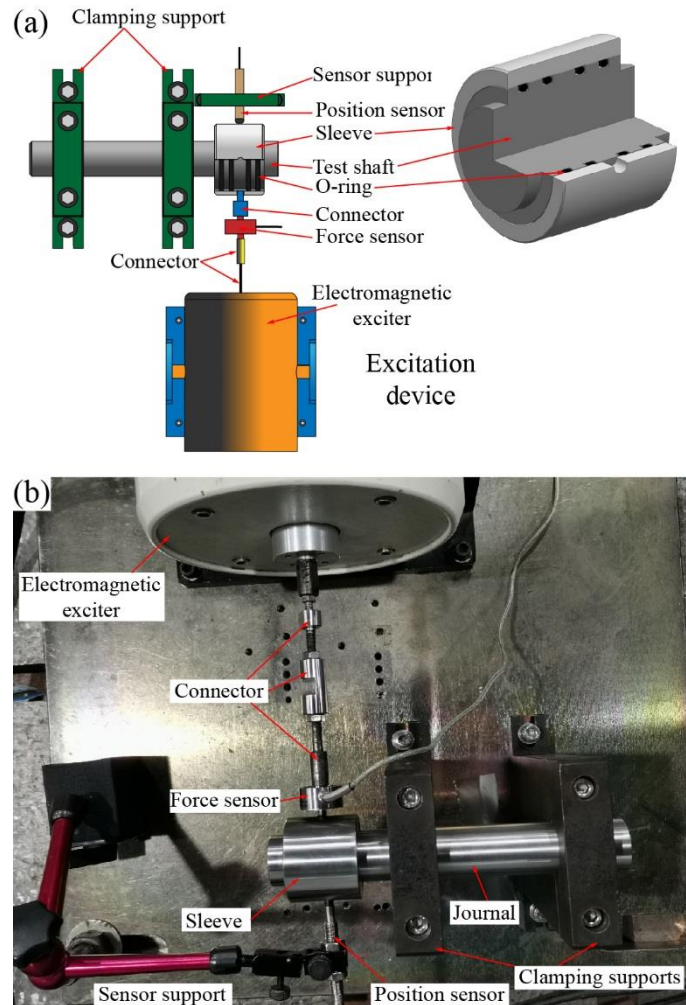


Figure 9 (a) Schematic diagram and (b) physical map of the excitation test-rig

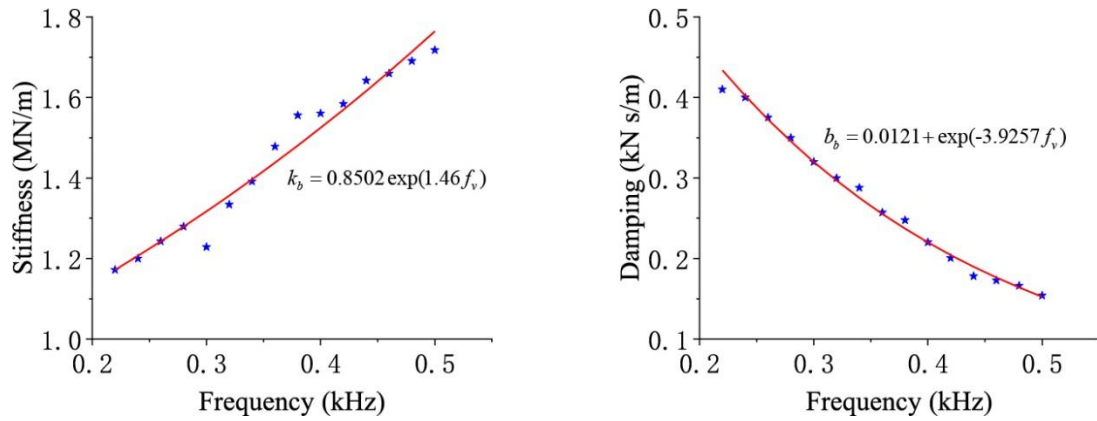


Figure 10 Stiffness and damping of an O-ring with the HNBR material varying with frequency

3.4 Comparison of the results of the theoretical and experimental analyses

With the tested values of the stiffness and damping of the O-rings in the numerical calculation, the numerical results of the vibration characteristics of the rotor can be obtained with consideration of the influence of the O-rings. The synchronous vibration of the rotor presented in Figure 8 is used to compare the numerically predicted results. The comparison is presented in Figure 11. The amplitude of the vibration is first increased and gradually decreased with the increase in rotational speed regardless of the variation of the external supply pressure. The critical speeds of the experimental and numerical results are well corresponded with a slight difference. The difference is caused by the experimental error. The idealized installation of the excitation test-rig must ensure that the centers of the new sleeve and journal are located on the excitation direction of the exciter. However, the installation error is inevitable, and it will cause the error of the measured stiffness and damping of the O-rings. The test-rig for the RPS experiment is complicated. The machine and installation errors are inevitable, which will also cause the error of the measured dynamic characteristics of the rotor. The stiffness and damping of the O-rings that are used in the numerical calculation are obtained on the basis of the excitation testing, and the error of the excitation testing will be brought into the numerical results. Therefore, the final difference between the numerical and the experimental results (Figure 11) is inevitable but acceptable, and it proves that the numerical model of the RPS coupled with the influence of O-rings is credible. Then, the numerical model will be used to extensively analyze the

characteristics of the RPS with different design and operating parameters.

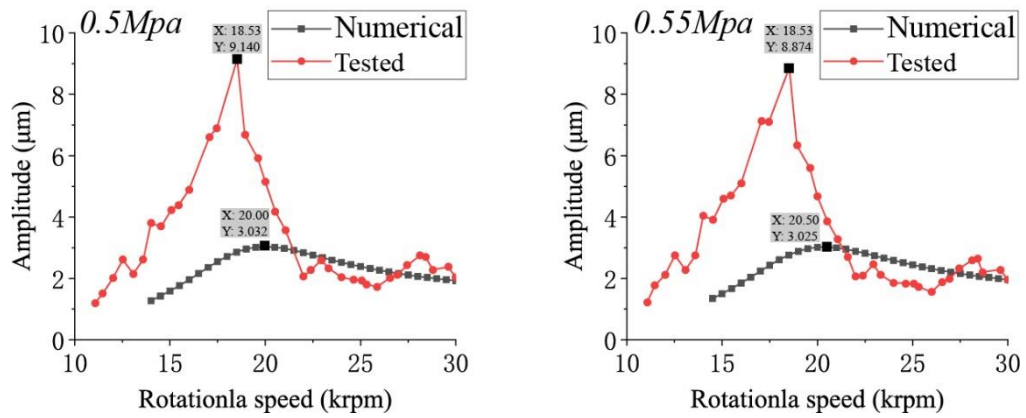


Figure 11 Comparison of the numerically calculated and experimentally tested synchronous amplitudes of the rotor in the vertical direction with a rotational speed of 12–30 krpm and external supply pressure values of 0.5 and 0.55 MPa

4 Results and discussion

This section mainly discusses the characteristics of the RPS coupled with the influence of the O-rings. The design and operating parameters include the material and number of the O-rings, the rotational speed of the rotor, the external supply pressure, the bearing clearance, and the porous permeability. The necessary abbreviations are presented for simplicity. The O-rings with the styrene butadiene rubber, methyl vinyl silicone rubber, and nitrile butadiene rubber as the materials are called SBRO, VMQO, and NBRO, respectively. The bearings with these three types of O-rings mounted are called BSBR, BVMQ, and BNBR, respectively. The bearing without O-ring mounted is called BR for simplicity.

Figure 12 shows the stiffness and damping of these three types of O-rings varying with frequency and the corresponding fitted formulas, which were experimentally tested by Miyanaga and Tomioka [27]. The stiffness and damping of the O-rings are substituted into the numerical model of the RPS. The other parameters, which are used in the numerical calculation, are listed in Table. 2. In the following text, the position of the rotor center relative to the center of the housing is represented by absolute vibration, absolute orbit, absolute position, or absolute response. The position of the rotor center relative to the center of the bearing is represented by relative vibration, relative orbit, relative position, or relative response.

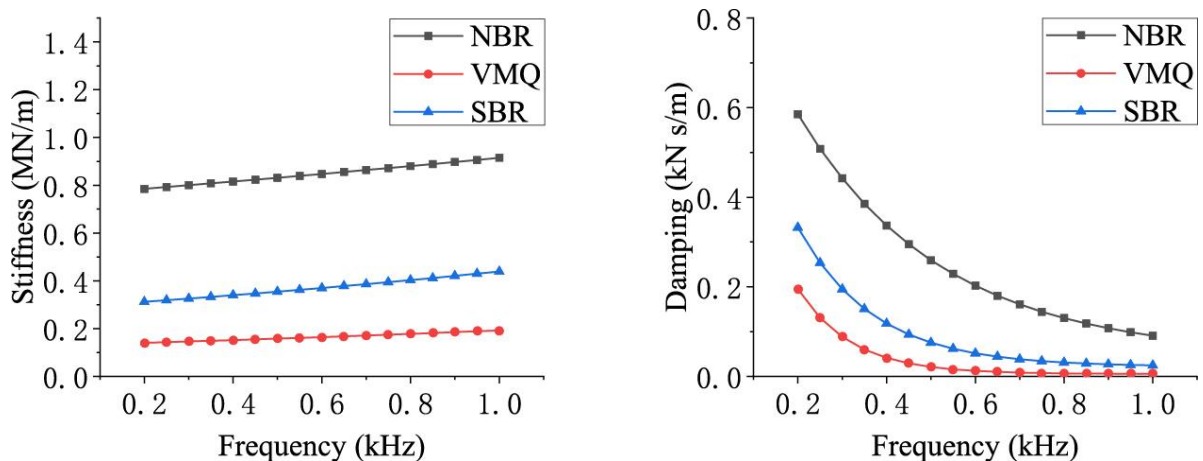


Figure 12 Empirical formulae for the three types of test O-rings in 0.2–1.0 kHz [27]

Table 2 Parameters for the numerical calculation

PAJB parameters	
Bearing mass, m_b	0.2 kg
Bearing diameter, D	25 mm
Bearing length, L	45 mm
Porous thickness, r_s	2.5 mm
Nominal clearance, h_0	10–30 μm
Porous carbon porosity ratio, η	0.1
Porous permeability, k	$0.1\text{--}2.0 \times 10^{-9} \text{ mm}^2$
Supply pressure, p_s / p_a	2–4
Rotor parameters	
Total mass, $2m_s$	2 kg
Mass eccentricity of the rotor, e_{ub}	2.83 μm
Rotational speed	12–60 krpm
Environmental parameters	
Ambient pressure, p_a	$1.01 \times 10^5 \text{ Pa}$
Air viscosity	$19.8 \times 10^{-6} \text{ Pa} \cdot \text{s}$
Temperature of the supplied air	294 K

4.1 Effects of O-rings with different materials

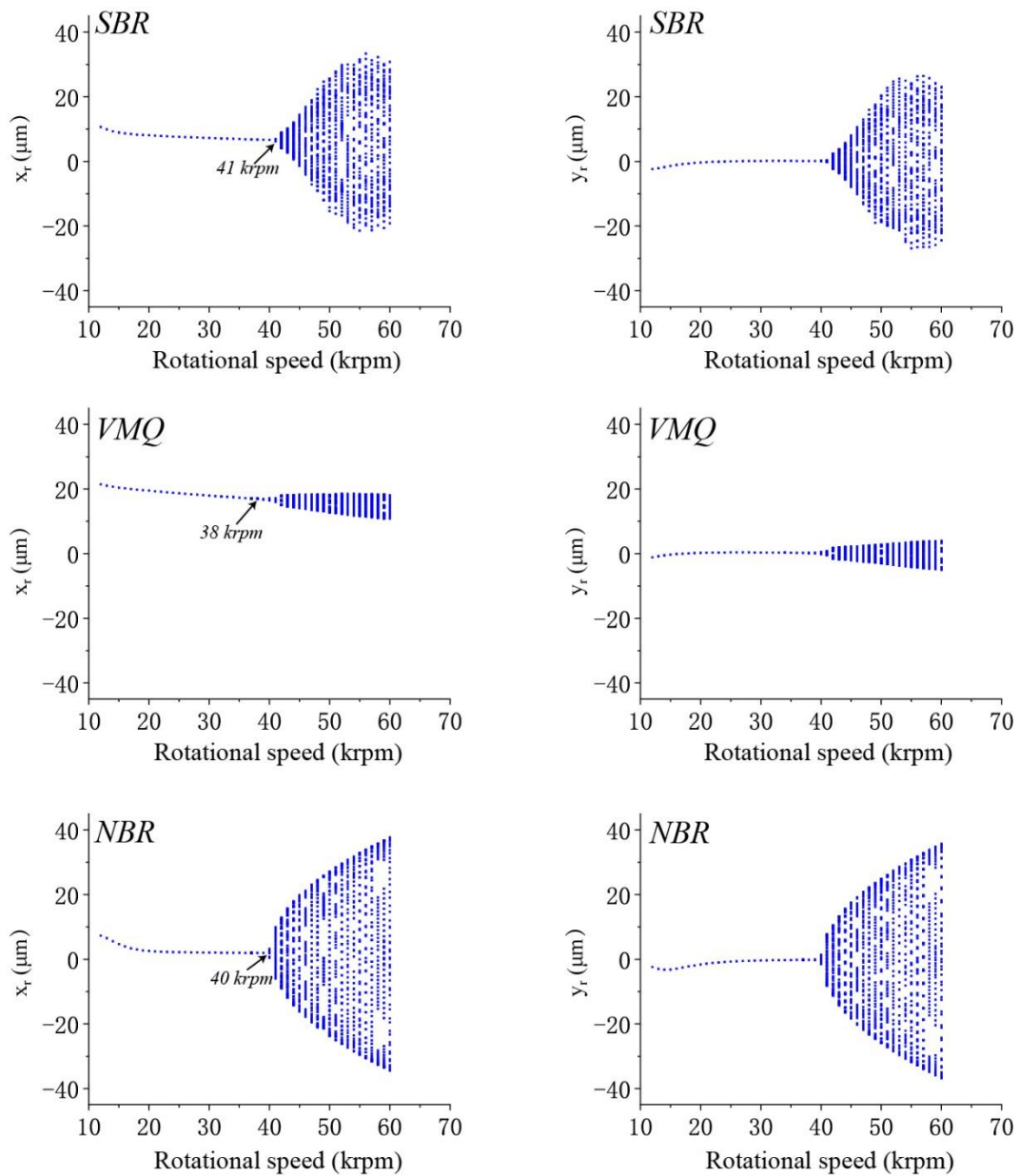


Figure 13 Bifurcation diagram of the absolute vibration of the rotor versus rotational speed (12–60 krpm) with rotor supported on BSBR, BVMQ, and BNBR

SBR, VMQ, and NBR are the three commonly used materials in obtaining O-rings. The effects of different O-rings, which are distinguished by materials, on the dynamic characteristics of RPS are discussed in this part. The bifurcation diagram of the absolute vibration of the rotor versus rotational speed (12–60 krpm) with different O-rings mounted is presented in Figure 13. The rotor absolute response in the vertical and horizontal directions with different O-rings show periodic motions in low rotational speed. The quasi-periodic responses are gradually determined with the increase in

rotational speed. The demarcation rotational speeds of the rotor absolute responses changed from periodic motions to quasi-periodic motions with the SBRO, VMQO, and NBRO mounted are 41, 38, and 40 krpm, respectively. When the rotational speed is lower than the demarcation rotational speed, the coordinate value of the rotor center absolute position in the x -direction is larger than that in y -direction. This phenomenon occurs because the gravity direction is along the x -direction. The absolute vibrations along the x - and y -directions are simultaneously decreased with the increase in rotational speed but not beyond the demarcation value. Specifically, the rotor center is gradually close to the center of the housing. This phenomenon occurs because the frequency of the excitation force that acts on the O-rings is increased with the increase in rotational speed, thereby resulting in the increase in the stiffness of the O-rings (Figure 12). With the rotational speed being lower than the demarcation value, the absolute coordinates along the x -direction are arranged from small to large in the following order: that of rotor supported by BNBR, BSBR, and BVMQ. This is because the stiffness of the O-rings when arranged in a descending order is that of NBRO, SBRO, and VMQO. The amplitude of the rotor absolute vibration for the bearings with SBRO mounted is smaller than that with NBRO mounted and larger than with VMQO mounted when the rotational speed is increased to be larger than the demarcation rotational speed.

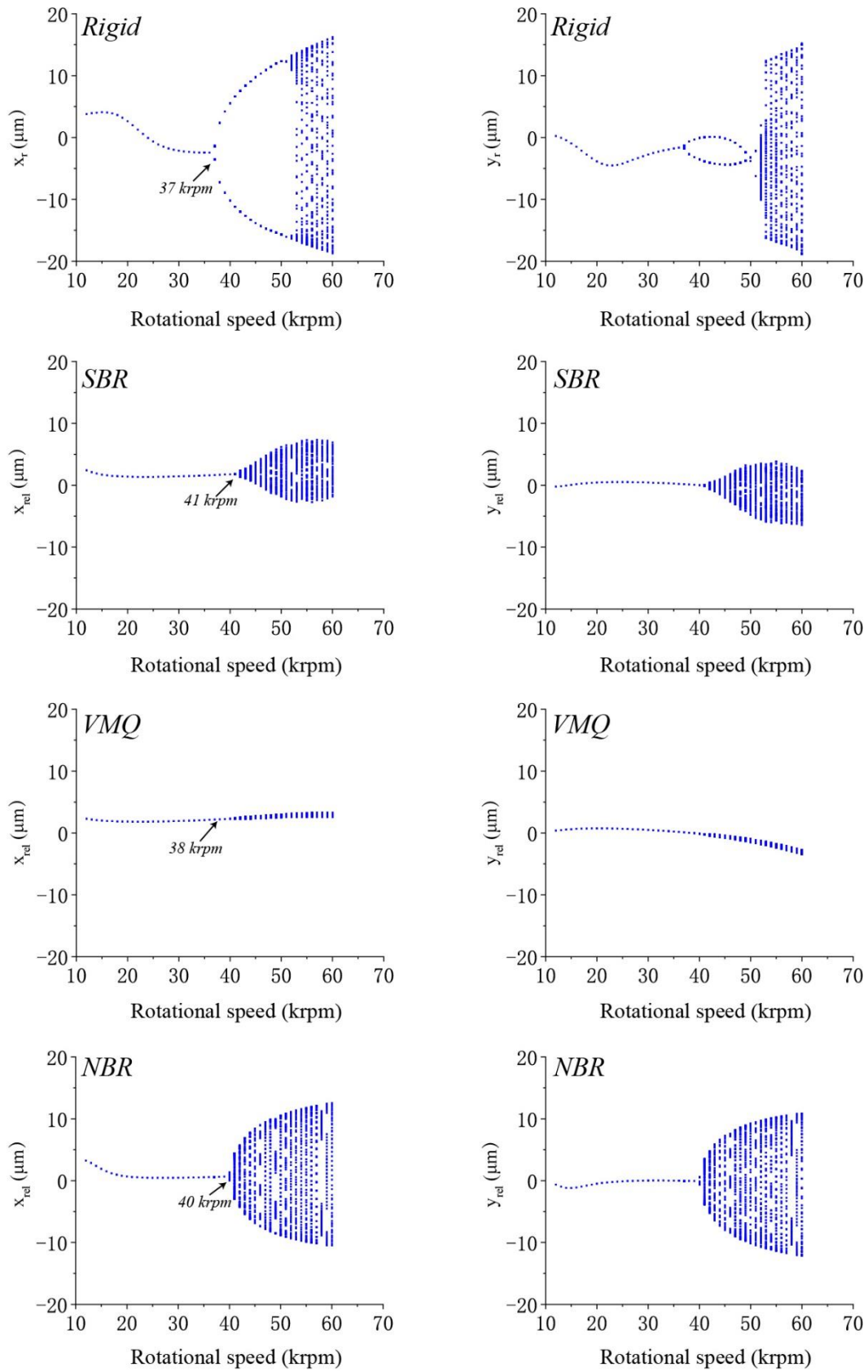
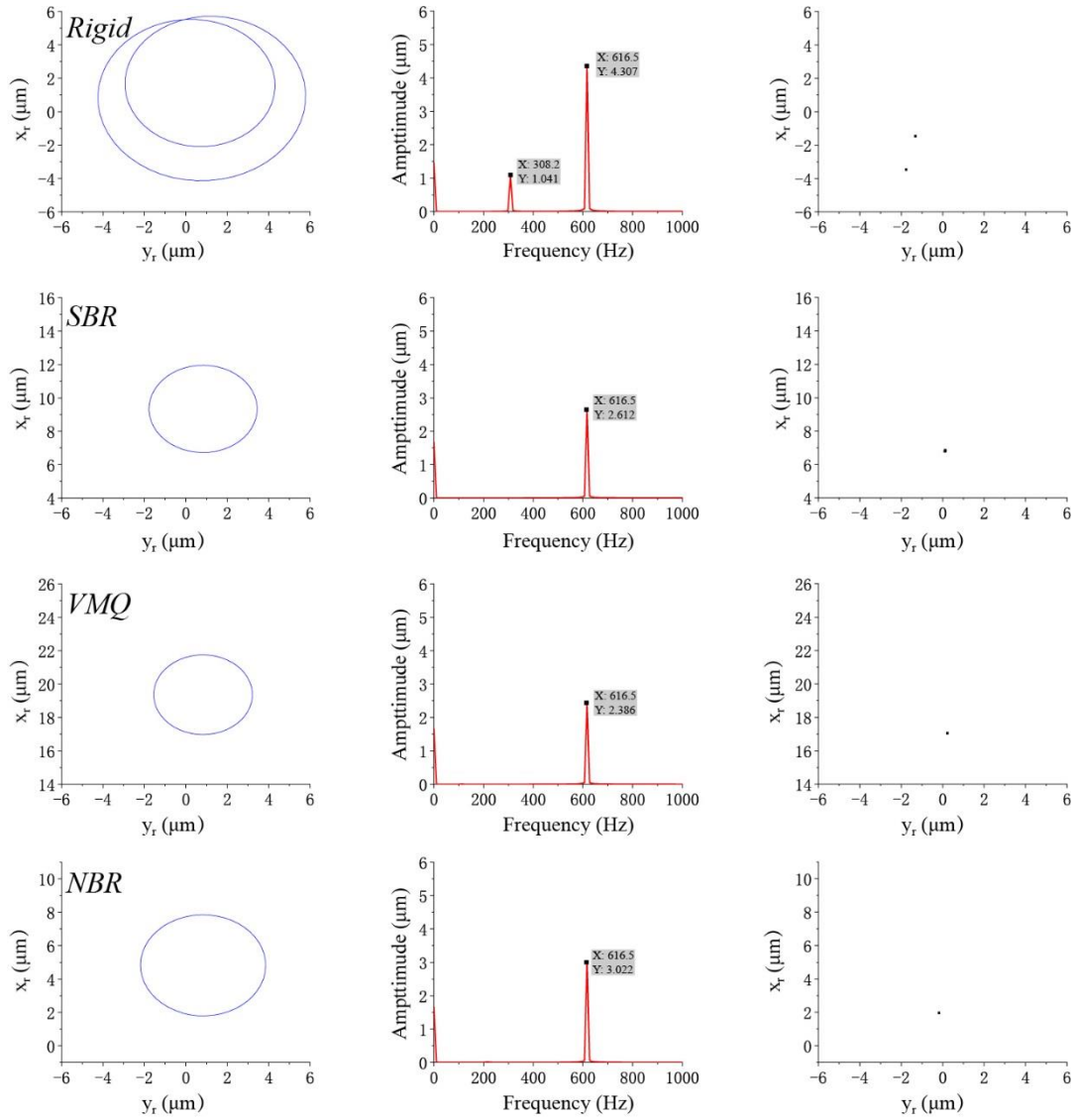
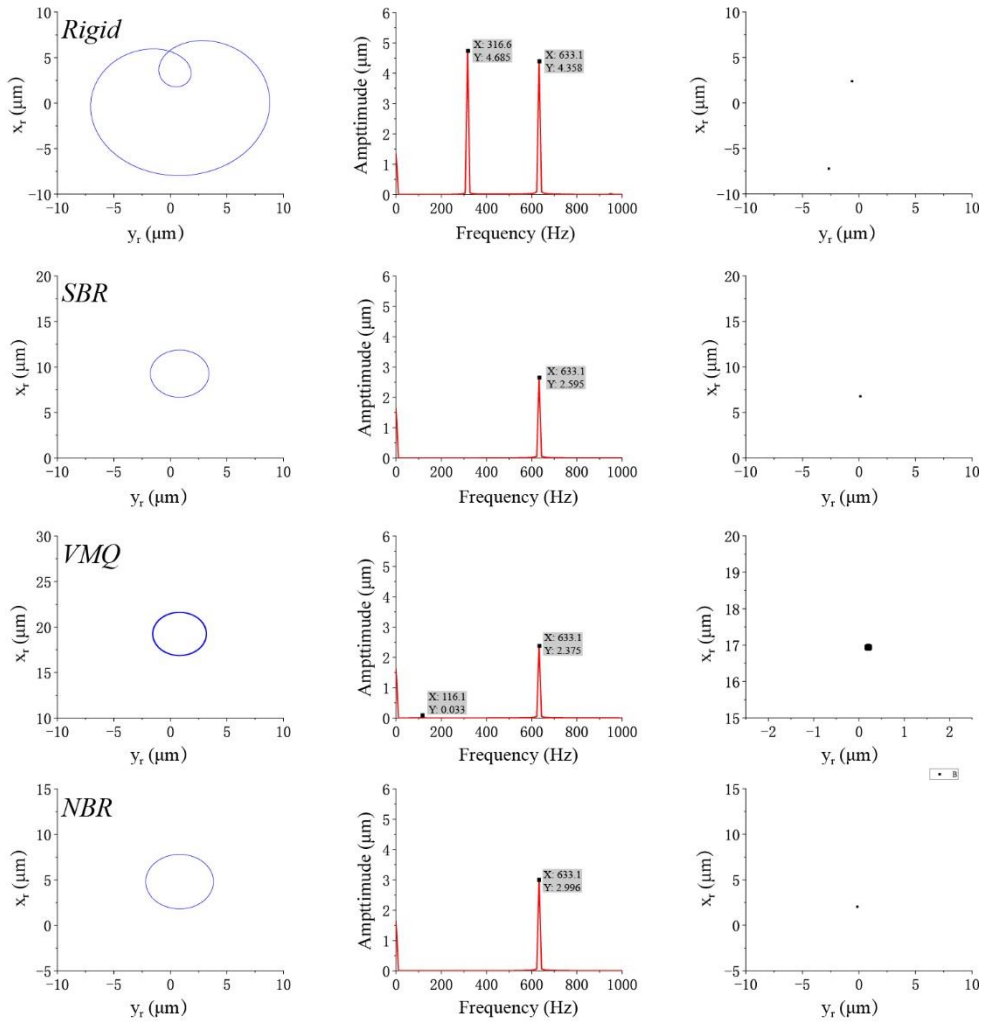


Figure 14 Bifurcation diagram of the relative vibration of the rotor versus rotational speed (12–60 krpm) when the rotor is supported on BR, SBR, VMQ, and NBR

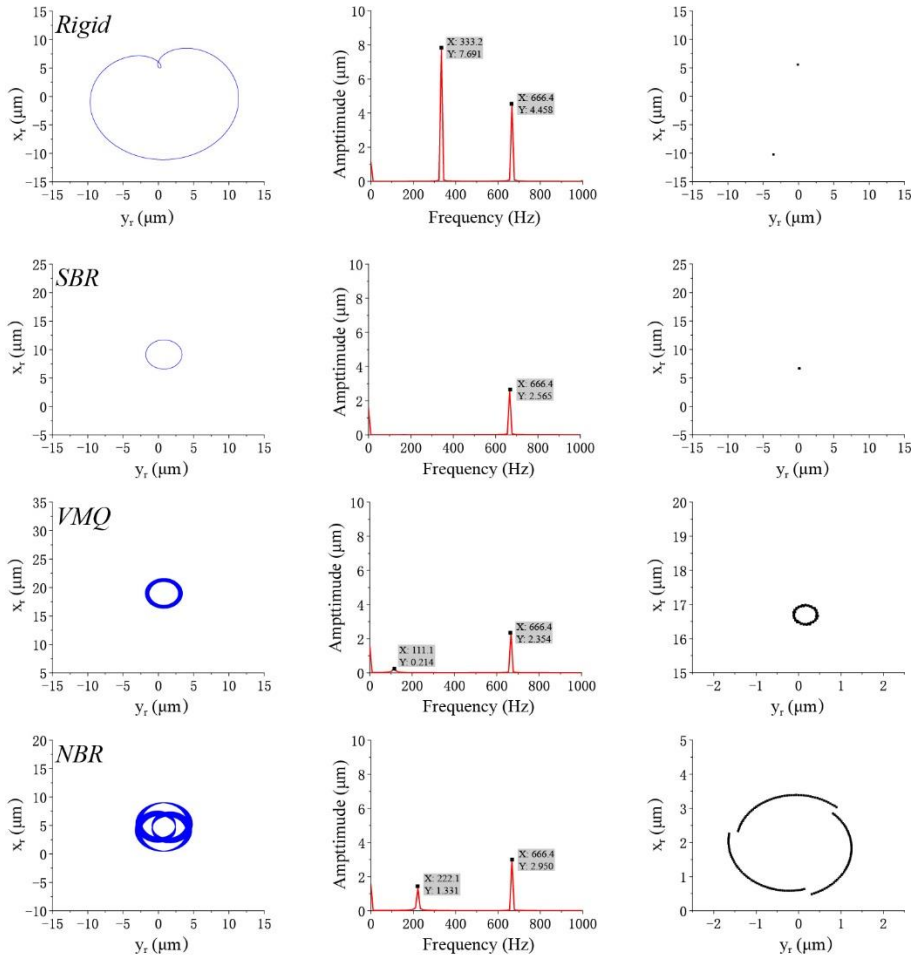
Figure 14 shows the bifurcation diagram of the relative vibration of the rotor versus rotational speed (12–60 krpm). The results for the O-rings mounted on the RPS with SBR, VMQ, and NBR materials are compared with the RPS that the bearing is rigid supported. The rotor relative responses are also changed from periodic motions to quasi-periodic motions with the increase in rotational speed, and the demarcation rotational speeds of the change for the rotor supported by SBRO, VMQO, and NBRO are also 41, 38, and 40 krpm respectively. Without O-ring mounted, the demarcation rotational speed is 37 krpm, and the vibration amplitude of the quasi-periodic motions is significantly higher than that with O-rings mounted. The relative vibration amplitude of the quasi-periodic motions for the RPS with SBRO mounted is higher than that with VMQO but lower than that with NBRO. Therefore, the effectiveness of O-rings in increasing the stability can be arranged from good to better in the following order: NBRO, SBRO, and VMQO. This characteristic is similar to the results presented in Ref. [25].



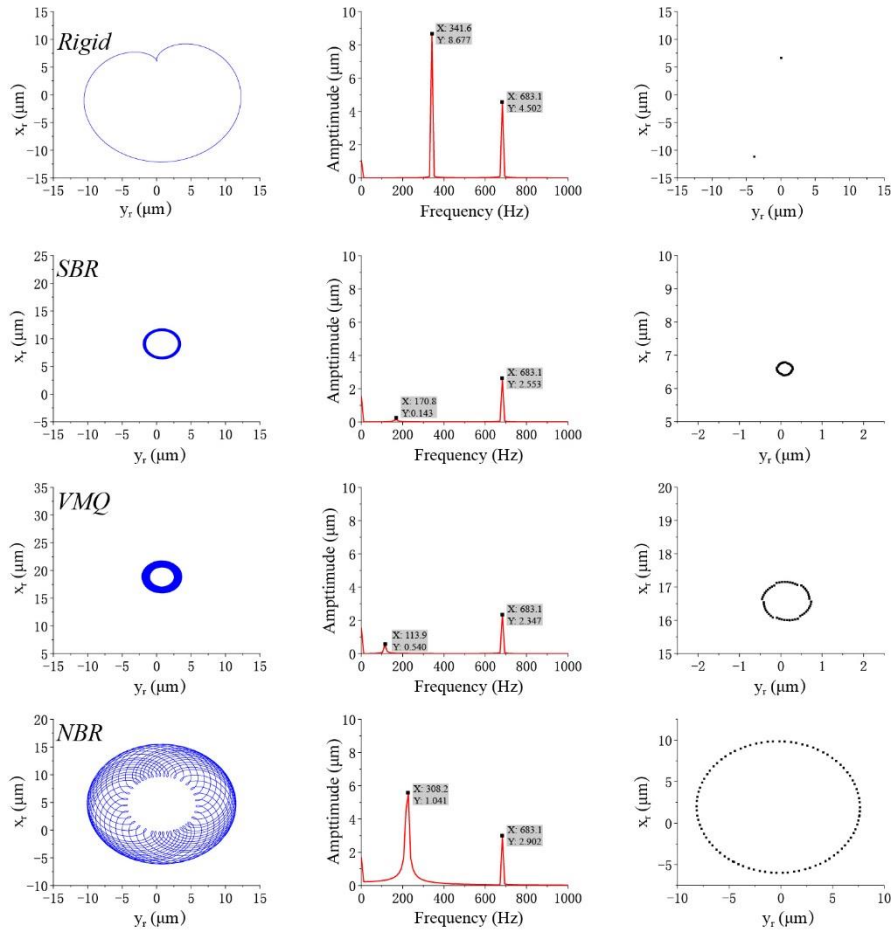
(a)



(b)



(c)



(d)

Figure 15 Predicted relative orbit and Poincaré maps of the rotor center and the FFT of the rotor center relative displacement in the horizontal direction with different rotational speeds: (a) 37, (b) 38, (c) 40, and (d) 41 krpm

The relative orbit and Poincaré maps of the rotor center and the FFT of the rotor relative displacement in the horizontal direction are presented for a clear understanding of the characteristics and dynamic responses of the RPS. Figure 15 shows the results for the rotors supported on BR, BNBR, BSBR, and BVMQ.

Figure 15(a) shows the results with the rotational speed of 37 krpm. With regarding to the characteristics of RPS without O-ring mounted, the orbit shape of the rotor is a regular curve with sub-synchronous vibration. The rotor performs quasi-periodic motions with a Poincaré map showing two points. The amplitudes of the sub-synchronous and synchronous vibrations are approximately 1.041 and 4.307 μm , respectively. With the O-rings mounted, all the orbit shapes of the rotors are closed

curves, the rotors performed periodic motions, and the Poincaré map exhibited a point. The orbit sizes and synchronous amplitudes are evidently smaller than those without O-ring mounted. Moreover, the orbit size and synchronous amplitude of the rotor supported on BSBR are larger than those on BVMQ and smaller than those on BNBR. The rotor supported on BR still performs quasi-periodic motions with the increase in rotational speed to 38 krpm, as shown in Figure 15(b). The orbit size and amplitude of the sub-synchronous and synchronous vibrations are increased. However, the rotor also performs quasi-periodic motions with the occurrence of sub-synchronous vibration when it is supported on BVMQ. The amplitude of the sub-synchronous vibration is approximately $0.033 \mu\text{m}$. The results of the rotors supported on BSBR and BNBR indicated that the relative orbit shapes are still closed curves. The relationship of the synchronous vibration amplitude of the rotor supported on different O-ring mounted bearings is the same as that presented in Figure 15(a). The comparison results presented in Figures 15(a) and 15(b) show that the synchronous vibration amplitude of the rotor is decreased with the increase in rotational speed for the RPS with O-rings mounted. Figure 15(c) shows that orbit size and vibration amplitude are continuously increased with the continuous increase in rotational speed to 40 krpm when the rotor is supported on BR. The amplitude of the sub-synchronous vibration becomes much higher than that of the synchronous vibration. The sub-synchronous vibration amplitude of the rotor supported on BVMQ is also increased. The rotor supported on BNBR also performs quasi-periodic motions with very high sub-synchronous vibration amplitude. The rotor still performs periodic motions when it is supported on BSBR. The synchronous vibration amplitudes of the rotor supported on O-ring mounted bearings are continuously decreased, and the relationship of the synchronous vibration amplitudes is also the same as that presented in Figure 15(a). Figure 15(d) presents the results with the rotational speed of 41 krpm. The rotor performs quasi-periodic motions in all the conditions. The amplitudes of the sub-synchronous vibration of the rotors supported on BR and BNBR are increased (nearly double that of the synchronous one). The synchronous vibration amplitude of the rotor is continually increased when it is supported on BR and decreased when supported on

O-ring mounted bearings with the increase in rotational speed from 40 krpm to 41 krpm. Moreover, the synchronous vibration amplitudes of the rotor supported on different O-rings mounted bearings have the relationship which is same as that presented in Figure 15(a).

4.2 Effects of the number of O-rings

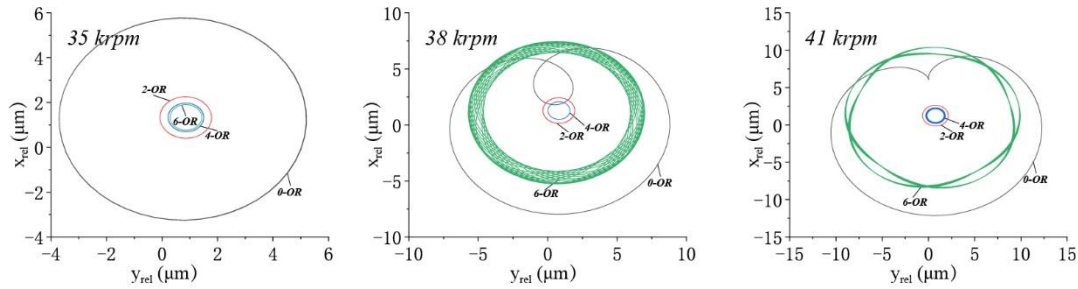


Figure 16 Predicted relative orbit of the rotor for the RPS with different numbers of SBRO mounted when the rotational speeds are 35, 38, and 41 krpm

In this part, the effects of the number of O-rings on the performance of the RPS are analyzed. Figure 16 shows the comparison of the relative orbit of the rotor with bearings mounted by different numbers of SBRO when the rotational speeds are 35, 38, and 41 krpm. The orbit shapes of the rotor are closed curves for all the conditions with the rotational speed of 35 krpm. Moreover, the orbit size is slightly decreased with the increase in the number of O-rings. When the rotational speed of the RPS with six O-rings mounted is increased to 38 krpm, the orbit size is significantly increased, and the rotor performs quasi-periodic motions. This phenomenon occurs because the total stiffness and damping of the six O-rings are quickly increased and decreased, respectively, with the increase in rotational speed. The orbit size of the RPS with four O-rings mounted is still smaller than that with two O-rings mounted. The total stiffness and damping of O-rings are continually increased and decreased, respectively, with the increase in the rotational speed to 41 krpm. Accordingly, the rotor performs quasi-periodic motions with four O-rings mounted in the RPS.

4.3 Effects of external supply pressure with O-rings mounted

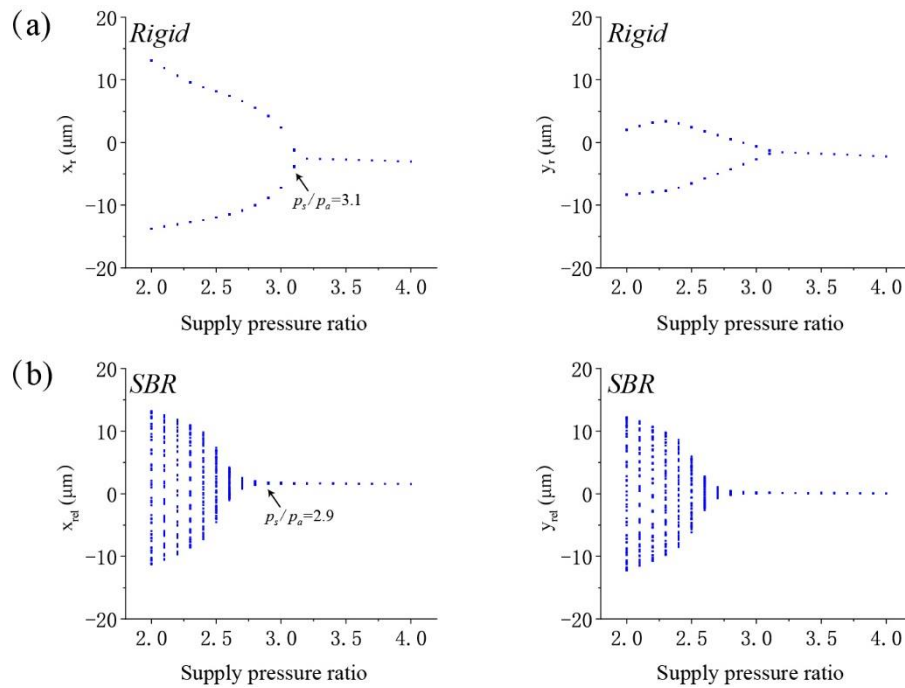


Figure 17 Bifurcation diagram of the relative vibration of the rotor versus external supply pressure (2–4 bar) when it is supported on (a) BR and (b) BSBR

Figure 17 shows the bifurcation diagram of the relative vibration of the rotor in the vertical and horizontal directions versus external supply pressure when it is supported on (a) BR and (b) BSBR. The rotors in two directions of the RPS with and without O-rings mounted perform quasi-periodic motions in the low external supply pressure. The rotor supported on BR shows a periodic motion with the increase in the external supply pressure to greater than 3.1 bar. This phenomenon occurred because increasing the external supply pressure can increase the stiffness of the air film to prevent rotor orbit divergency. The performance of the BSBR supported rotor is also changed from quasi-periodic motion to periodic motion with the increase in the external supply pressure, and the demarcation pressure is 2.9, which is lower than that of the rotor supported on BR. This situation persisted because the elastic suspension can increase the stability of the RPS.

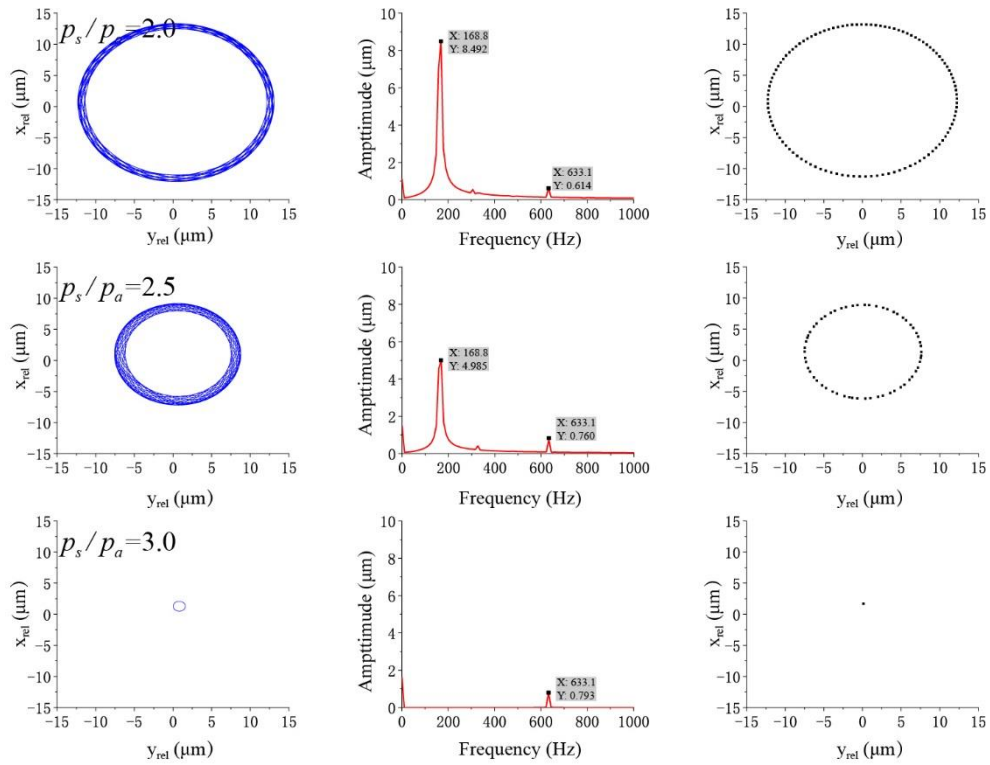


Figure 18 Predicted relative orbit and Poincaré maps of the rotor center and FFT of the rotor center relative displacement in the horizontal direction with different supply pressure values

Figure 18 shows the predicted relative orbit and Poincaré maps of the rotor center and the FFT of the rotor center relative displacement in the horizontal direction with supply pressure values of 2.0, 2.5, and 3.0 bar. The rotor is supported on BSR. The orbit size is gradually decreased with the increase in the external supply pressure, and the orbit shape is changed from regular curves to closed curve. The rotor motion is changed from quasi-periodic to periodic with the Poincaré map changing from a circle to a point. The amplitude of the sub-synchronous vibration is very high with a supply pressure of 2.0 bar. The value is quickly decreased and finally disappeared with the increase in the external supply pressure. However, the synchronous amplitude is less influenced by the external supply pressure. The amplitude only slightly increased at high external supply pressure. The results are similar to those in Ref. [14]

4.4 Effects of bearing clearance with O-rings mounted

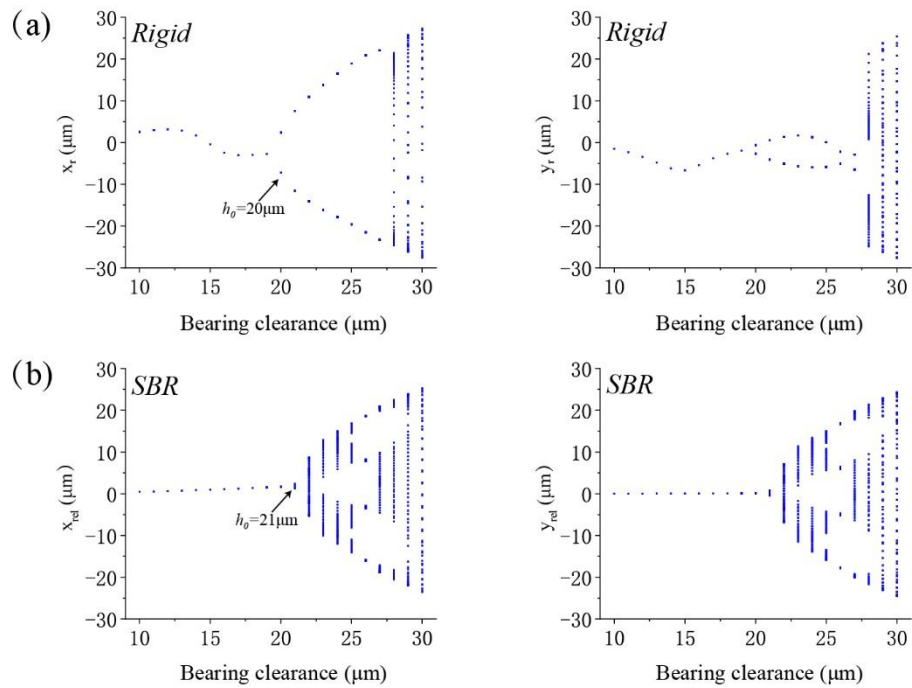


Figure 19 Bifurcation diagram of the relative vibration of the rotor versus the bearing clearance (10–30 μm) when it is supported on (a) BR and (b) BSBR

Figure 19 shows the bifurcation diagram of the relative vibration of the rotor in the vertical and horizontal directions versus the bearing clearance when it is supported on (a) BR and (b) BSBR. The rotor motion is periodic at small clearance. Then, such motion changed to a quasi-periodic one with the increase in clearance. This phenomenon occurred because increasing clearance decreases the film stiffness. The demarcation clearance to change the rotor motion from periodic to quasi-periodic is 20 μm for the rotor supported on BR, and it is increased to 21 μm for the rotor supported on BSBR.

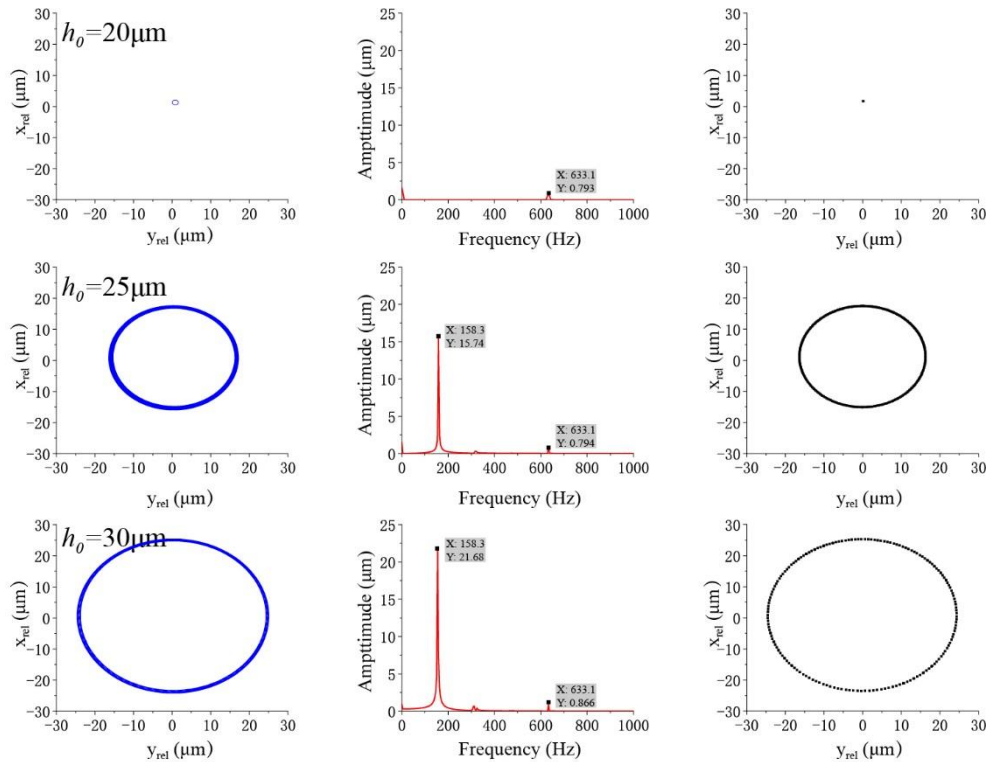


Figure 20 Predicted relative orbit and Poincaré map of the rotor center and the FFT of the rotor center relative displacement in the horizontal direction with different bearing clearances

Figure 20 shows the predicted relative orbit and Poincaré maps and the FFT of the rotor center relative displacement in the horizontal direction with bearing clearances of 20, 25, and 30 μm . The rotor is supported on BSBR. The orbit shape shows a closed curve, and the rotor motion is periodic with the Poincaré map showing a point when the clearance is 20 μm . The orbit size is significantly increased with the increase in clearance to 25 μm , and its shape is changed to a regular curve. The comparison of the results with the clearances of 20 and 25 μm shows that the amplitude of the synchronous vibration is nearly not changed. However, sub-synchronous vibration occurred, and its amplitude is very high. The rotor motion is changed to a quasi-periodic one when the Poincaré map is a smooth circle. The orbit shape, the amplitude of synchronous vibration, and the Poincaré map of the rotor are nearly not changed with the continued increase in clearance to 30 μm relative to the results with a clearance of 25 μm . However, the orbit size and the amplitude of the sub-synchronous vibration are significantly increased.

4.5 Effects of material permeability with O-rings mounted

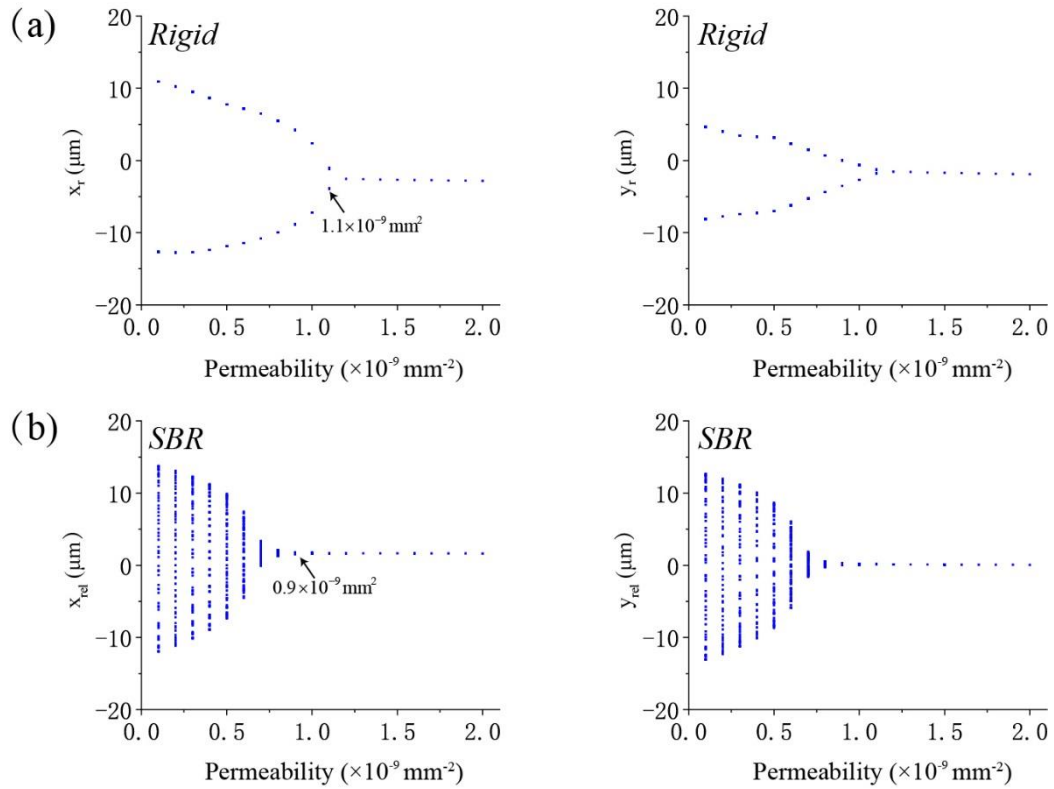


Figure 21 Bifurcation diagram of the relative vibration of the rotor versus porous permeability ($0.1 \times 10^{-9} - 2 \times 10^{-9} \text{ mm}^{-2}$) when it is supported on (a) BR and (b) BSBR. Figure 21 shows the bifurcation diagram of the relative vibration of the rotor in the vertical and horizontal directions versus the porous permeability when it is supported on (a) BR and (b) BSBR. The rotor center in two directions always shows a quasi-periodic motion with smaller permeability. The film force can be increased with the increase in permeability, which increases the bearing stiffness, thereby resulting in the rotor center gradually showing a periodic motion. This finding is similar to the results with the influence of external supply pressure. Although a higher permeability can increase the stability of RPS, the air hammer of the porous air bearings may occur with the increasing in permeability. The demarcation permeabilities are 1.1×10^{-9} and $0.9 \times 10^{-9} \text{ mm}^{-2}$ when the rotor is supported on BR and BSBR, respectively. This result means that the whirl stability of the O-rings mounted RPS can be ensured at a lower permeability to efficiently prevent the air hammer.

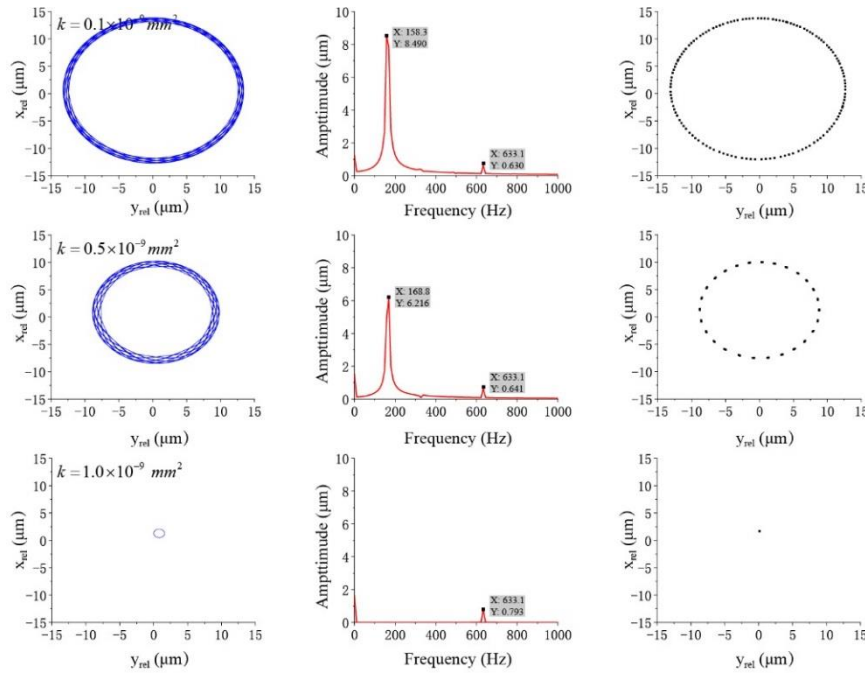


Figure 22 Predicted relative orbit and Poincaré map of the rotor center and the FFT of the rotor center relative displacement in the horizontal direction with different porous permeabilities

Figure 22 shows the predicted relative orbit and Poincaré maps and the FFT of the rotor center relative displacement in the horizontal direction with porous permeabilities of 0.1×10^{-9} , 0.5×10^{-9} , and $1.0 \times 10^{-9} \text{ mm}^{-2}$. The rotor is supported on BSR. The orbit shape shows a regular curve with a large orbit size and very high amplitude of the sub-synchronous vibration when the porous permeability is $0.1 \times 10^{-9} \text{ mm}^{-2}$. The amplitude of the synchronous vibration is smaller compared with that of the sub-synchronous vibration. Moreover, the rotor shows a quasi-periodic motion with the Poincaré map showing a nearly closed curve. The orbit shape is still a regular curve when the porous permeability is increased to $0.5 \times 10^{-9} \text{ mm}^{-2}$. However, the orbit size and amplitude of the sub-synchronous vibration are decreased. The amplitude of the synchronous vibration is still smaller than that of the sub-synchronous vibration, but it is increased. The rotor also shows quasi-periodic motion with the Poincaré map showing a dashed circle. The orbit shape is changed to a closed curve with a small size with the continued increase of the permeability to $1.0 \times 10^{-9} \text{ mm}^{-2}$, and the sub-synchronous vibration disappeared. The amplitude of the synchronous vibration is continually increased. However, the rotor shows a periodic motion with the Poincaré map showing a point.

5 Conclusion

This study presents a nonlinear analysis of the RPS with O-rings mounted. The lubrication film is modeled by combining Darcy's law and motion equation of air. The mechanical property of the O-rings is described by using the Voigt model with consideration of the influence of excitation frequency. The performance of RPS is modeled by considering the interaction of rotor, bearings, and O-rings. The numerical model is experimentally confirmed. The mechanical property of O-rings with the HNBR as the material is first obtained in the excitation test-rig. The tested stiffness and damping of the O-rings are substituted into the numerical model of RPS. Meanwhile, the tested O-rings are used in the rotor-bearing test-rig. The numerical and experimental test results of the performance of RPS are compared. Both results obtain good correspondence. Then, the characteristics of the RPS are analyzed by using bifurcation diagrams, orbit, Poincaré maps, and FFT plots. The effect of different system parameters, including the material of O-rings, number of O-rings, external supply pressure, bearing clearance, and porous permeability, on the performance of RPS are studied.

The influence of O-rings with SBR, VMQ, and NBR materials on the performance of RPS is first studied by simultaneously analyzing the absolute and relative responses of the rotor. The results show that the rotor motions are changed from periodic to quasi-periodic with the increase in rotational speed. During this process, the orbit shape becomes a regular curve with the increase in orbit size, and sub-synchronous vibration occurs. Meanwhile, the Poincaré map is changed from a point to several points. The demarcation rotational speeds for the motion change from periodic to quasi-periodic are 37, 41, 38, and 40 krpm with the rotor supported on BR, BSBR, BVMQ, and BNBR, respectively. Under the conditions of quasi-periodic motion, the orbit sizes and synchronous and sub-synchronous amplitudes of the rotor are significantly decreased with O-rings mounted. Thus, O-rings can increase the stability of RPS, and the effectiveness is arranged from good to better as follows: NBRO, SBRO, and VMQO.

Then, the effects of the other system parameters on the performance of RPS are studied on the basis of the rotor supported on BSBR by analyzing the relative motion of the

rotor. With the rotor performs periodic motions, the orbit size is slightly decreased with the increase in the number of O-rings. However, increasing the number of O-rings causes the rotor in easily performing quasi-periodic motions relative to the conditions with fewer number of O-rings but not zero at higher rotational speed condition. Once the quasi-periodic motion performs, the orbit size is significantly increased. Increasing the external supply pressure can make the quasi-periodic motioned rotor gradually perform periodic motion. The orbit size and vibration amplitude of sub-synchronous are significantly decreased with the increase in external supply pressure. The demarcation external supply pressure for motion type change is decreased with O-rings mounted. Increasing the bearing clearance significantly increases the orbit size and vibration amplitude of sub-synchronous to decrease the stability of RPS, and the rotor motion is changed from periodic to quasi-periodic motions. With the rotor supported on the O-rings mounted bearings, the demarcation clearance, which changes the rotor motion between periodic and quasi-periodic, is increased. The rotor performance shows a quasi-periodic motion at smaller porous permeability. Then, such performance gradually demonstrated a periodic motion with the increase in permeability. Moreover, increasing the permeability causes the orbit size and vibration amplitude of the sub-synchronous being significantly decreased. The demarcation permeability of the change is decreased with O-rings mounted.

Acknowledgments

The authors acknowledge the financial support by National Natural Science Foundation of China (Grant No. 52005170), Natural Science Foundation of Hunan Province (2020JJ5065), National Key R&D Program of China (2020YFB2007600), the Foundation of China Academy of Space Technology (CAST), the Fundamental Research Funds for the Central Universities, China, The Presidential Foundation of China Academy of Engineering Physics (YZJLX2018010).

Declarations:

The authors declare that they have no conflict of interest. All authors have approved the manuscript and agreed with submission to Nonlinear Dynamics.

Data Availability Statement

The datasets generated during and/or analysed during the current study are available from the corresponding author on reasonable request.

References

- [1] G. Chen, B. Ju, H. Fang, Y. Chen, N. Yu, and Y. Wan, "Air bearing: academic insights and trend analysis," *The International Journal of Advanced Manufacturing Technology*, vol. 106, pp. 1191-1202, 2020.
- [2] Q. Gao, W. Chen, L. Lu, D. Huo, and K. Cheng, "Aerostatic bearings design and analysis with the application to precision engineering: State-of-the-art and future perspectives," *Tribology International*, vol. 135, p. 17, 2019.
- [3] L. San Andrés, J. Yang, and A. Devitt, "On Tilting Pad Carbon-Graphite Porous Journal Bearings: Measurements of Imbalance Response and Comparison to Predictions of Bearing Performance and System Dynamic Response," *Tribology Transactions*, pp. 1-17, 2021.
- [4] K. Gururajan and J. Prakash, "Roughness effects in a narrow porous journal bearing with arbitrary porous wall thickness," *International Journal of Mechanical Sciences*, vol. 44, pp. 1003-1016, 2002.
- [5] K. Yamada, N. Onishi, K. Sekiya, and Y. Yamane, "Permeability control method with laser for porous bushings of aerostatic bearings," *International Journal of Precision Engineering and Manufacturing*, vol. 14, pp. 779-784, 2013.
- [6] T. H. Panzera, A. L. Christoforo, J. C. Campos Rubio, C. R. Bowen, P. H. R. Borges, and L. J. Silva, "Evaluation of Compacted Cementitious Composites for Porous Bearings," *International Journal of Applied Ceramic Technology*, vol. 10, pp. 474-483, 2013.
- [7] L. J. da Silva, T. H. Panzera, L. M. Vieira, J. G. Duduch, C. R. Bowen, and J. C. Campos Rubio, "Carbon nanotubes and superplasticizer reinforcing cementitious composite for aerostatic porous bearing," *Proceedings of the Institution of Mechanical Engineers, Part J: Journal of Engineering Tribology*, vol. 231, pp. 1397-1407, 2017.
- [8] Y. Otsu, M. Miyatake, and S. Yoshimoto, "Dynamic characteristics of aerostatic porous journal bearings with a surface-restricted layer," *Journal of Tribology*, vol. 133, p. 011701, 2011.
- [9] M. Miyatake, S. Yoshimoto, and J. Sato, "Whirling instability of a rotor supported by aerostatic porous journal bearings with a surface-restricted layer," *Proceedings of the Institution of Mechanical Engineers, Part J: Journal of Engineering Tribology*, vol. 220, pp. 95-103, 2006.
- [10] J. S. Jacob, J. Yu, D. E. Bently, and P. Goldman, "Air-hammer instability of externally pressurized compressible-fluid bearings," *Proc. ISCORMA*, vol. 1, pp. 20-24, 2001.
- [11] W. Liu, K. Feng, Y. Huo, and Z. Guo, "Measurements of the Rotordynamic Response of a Rotor Supported on Porous Type Gas Bearing," *Journal of Engineering for Gas Turbines and Power*, vol. 140, p. 102501, 2018.
- [12] C.-C. Wang, C.-Y. Lo, and C. o.-K. Chen, "Nonlinear dynamic analysis of a flexible rotor supported by externally pressurized porous gas journal bearings," *J. Trib.*, vol. 124, pp. 553-561, 2002.
- [13] X. Zhu and L. San Andrés, "Rotordynamic performance of flexure pivot hydrostatic gas bearings for oil-free turbomachinery," 2007.
- [14] Y. Wu, K. Feng, Y. Zhang, W. Liu, and W. Li, "Nonlinear dynamic analysis of a rotor-bearing system with porous tilting pad bearing support," *Nonlinear Dynamics*, vol. 94, pp. 1391-1408, 2018.
- [15] A. Delgado and B. Ertas, "Dynamic Characterization of a Novel Externally Pressurized Compliantly Damped Gas-Lubricated Bearing With Hermetically Sealed Squeeze Film Damper Modules," *Journal of Engineering for Gas Turbines and Power*, vol. 141, 2019.

- [16] Y. Gu, Y. Ma, and G. Ren, "Stability and vibration characteristics of a rotor-gas foil bearings system with high-static-low-dynamic-stiffness supports," *Journal of sound and Vibration*, vol. 397, pp. 152-170, 2017.
- [17] B. H. Ertas, "Compliant hybrid journal bearings using integral wire mesh dampers," *Journal of Engineering for Gas Turbines and Power*, vol. 131, 2009.
- [18] W. Liu, K. Feng, and P. Lyu, "Bifurcation and nonlinear dynamic behaviours of a metal mesh damped flexible pivot tilting pad gas bearing system," *Nonlinear Dynamics*, vol. 91, pp. 655-677, 2018.
- [19] P. Bättig and J. Schiffmann, "Flexible Support for Gas-Lubricated Bearing Bushings," *Tribology Transactions*, vol. 63, pp. 494-508, 2020.
- [20] N. Miyanaga and J. Tomioka, "Effect of support stiffness and damping on stability characteristics of herringbone-grooved aerodynamic journal bearings mounted on viscoelastic supports," *Tribology International*, vol. 100, pp. 195-203, 2016.
- [21] N. Shabaneh and J. W. Zu, "Nonlinear dynamic analysis of a rotor shaft system with viscoelastically supported bearings," *J. Vib. Acoust.*, vol. 125, pp. 290-298, 2003.
- [22] J. Dutt, "A simple Viscoelastic model of Rotor-Shaft Systems," in *IUTAM Symposium on emerging trends in rotor dynamics*, 2011, pp. 143-151.
- [23] S. Dousti, J. A. Kaplan, F. He, and P. E. Allaire, "Elastomer O-rings as centering spring in squeeze film dampers: Application to turbochargers," in *ASME Turbo Expo 2013: Turbine Technical Conference and Exposition*, 2013.
- [24] T. Waumans, J. Peirs, F. Al-Bender, and D. Reynaerts, "Aerodynamic journal bearing with a flexible, damped support operating at 7.2 million DN," *Journal of Micromechanics and Microengineering*, vol. 21, p. 104014, 2011.
- [25] G. Belforte, F. Colombo, T. Raparelli, and V. Viktorov, "High-speed rotor with air bearings mounted on flexible supports: test bench and experimental results," *Journal of tribology*, vol. 130, 2008.
- [26] G. Belforte, T. Raparelli, V. Viktorov, and F. Colombo, "An Experimental Study on a High-Speed Rotor Supported by Air Bearings Mounted on O-Rings," in *Engineering Systems Design and Analysis*, 2006, pp. 995-1000.
- [27] N. MIYANAGA and J. TOMIOKA, "Stability Threshold of Herringbone-Grooved Aerodynamic Journal Bearings with Considering Frequency Dependence of External Stiffness and Damping Elements," *JOURNAL OF JAPAN SOCIETY FOR DESIGN ENGINEERING*, p. 2015.2659, 2016.
- [28] J. Tomioka and N. Miyanaga, "Measurement of dynamic properties of O-rings and stability threshold of flexibly supported herringbone grooved aerodynamic journal bearings," *Tribology Online*, vol. 3, pp. 366-369, 2008.
- [29] N. Aktürk and R. Gohar, "Damping the vibrations of a rigid shaft supported by ball bearings by means of external elastomeric O-ring dampers," *Proceedings of the Institution of Mechanical Engineers, Part J: Journal of Engineering Tribology*, vol. 208, pp. 183-190, 1994.
- [30] L. San Andrés, K. Ryu, and T. H. Kim, "Identification of structural stiffness and energy dissipation parameters in a second generation foil bearing: effect of shaft temperature," *Journal of engineering for gas turbines and power*, vol. 133, p. 032501, 2011.

Figures

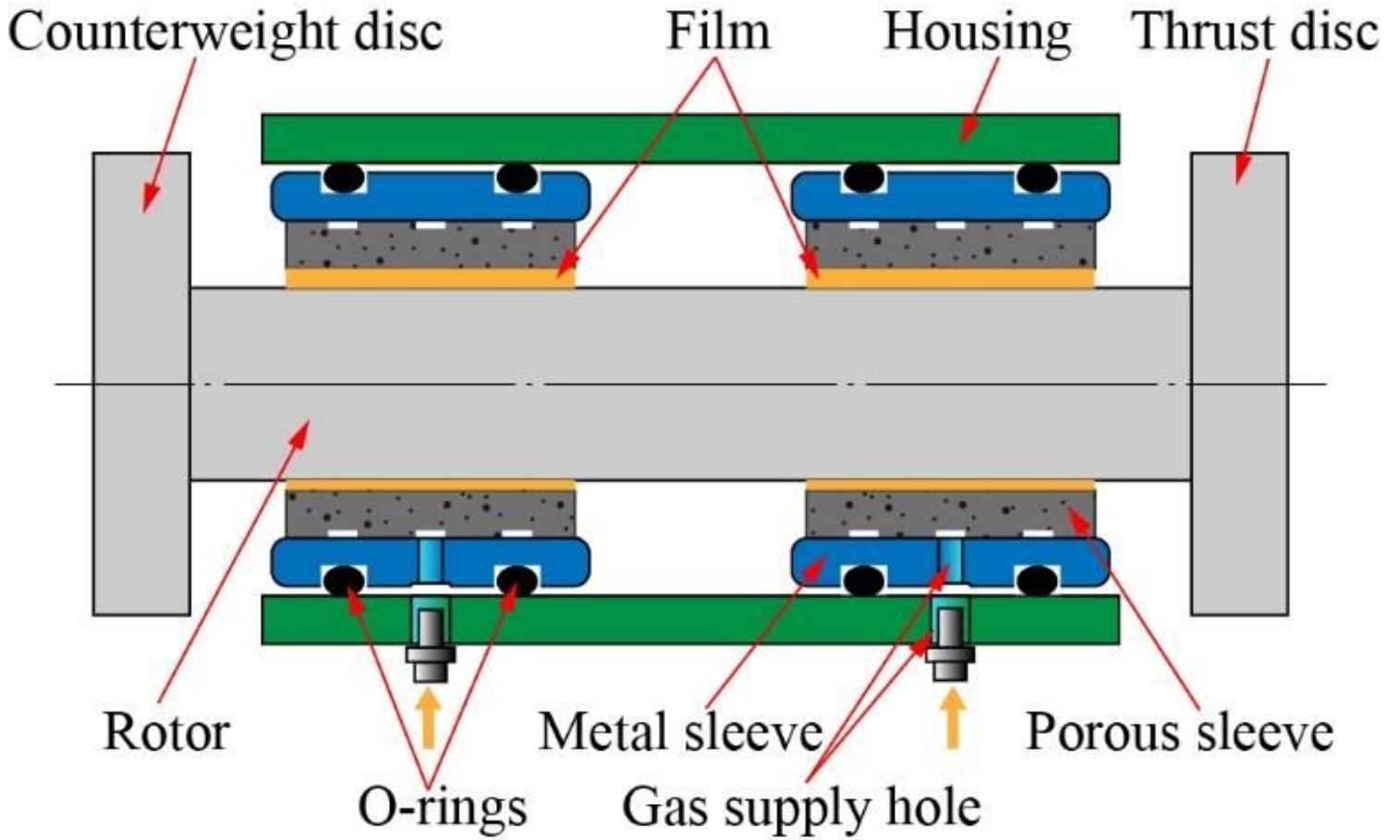


Figure 1

Schematic of the RPS with O-rings mounted

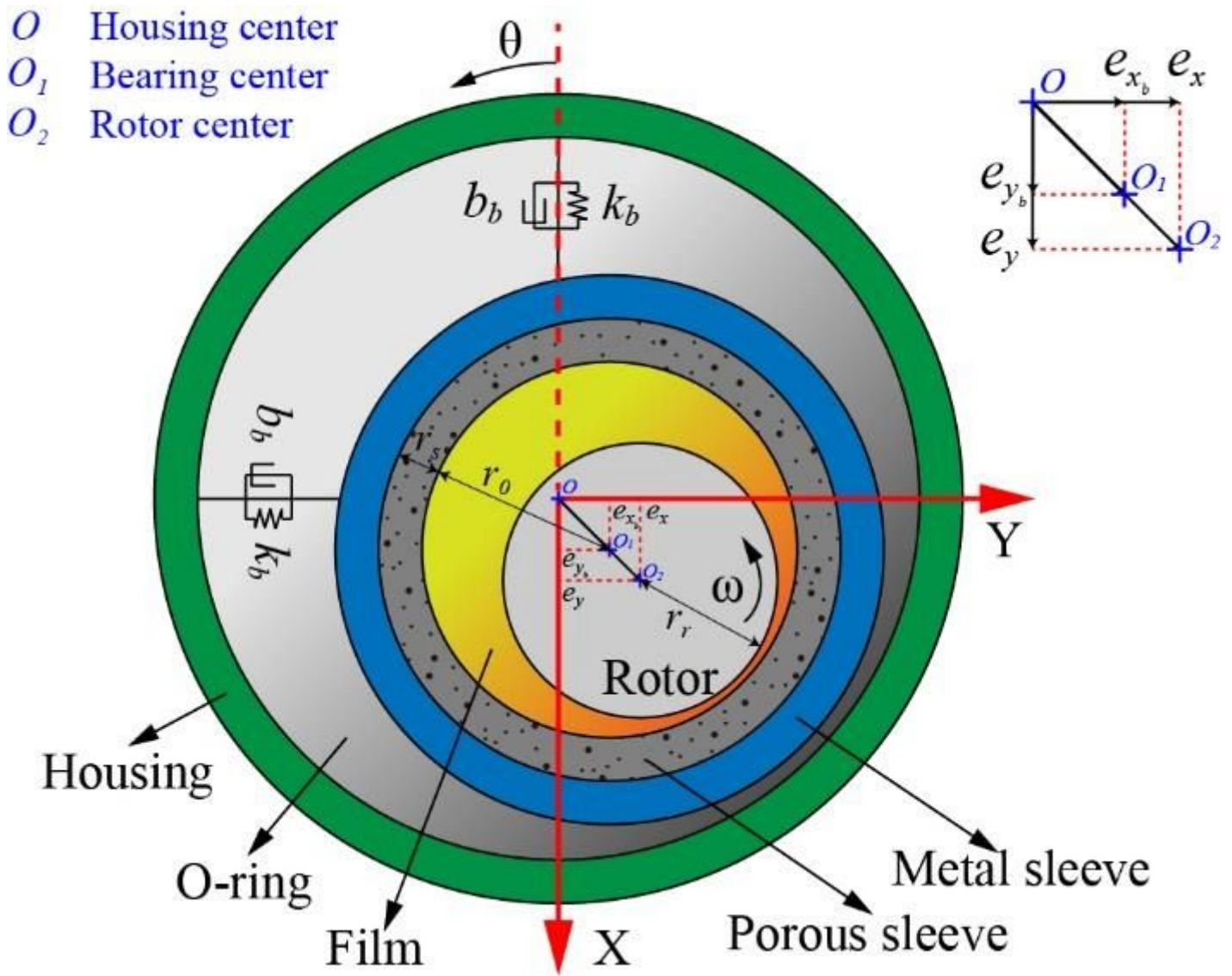
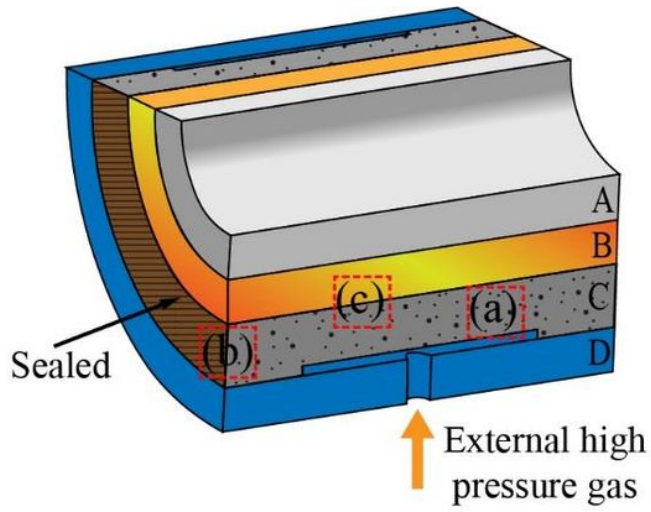


Figure 2

Geometric model of a PAJB



A--Rotor
 B--Film
 C--Porous sleeve
 D--Metal sleeve

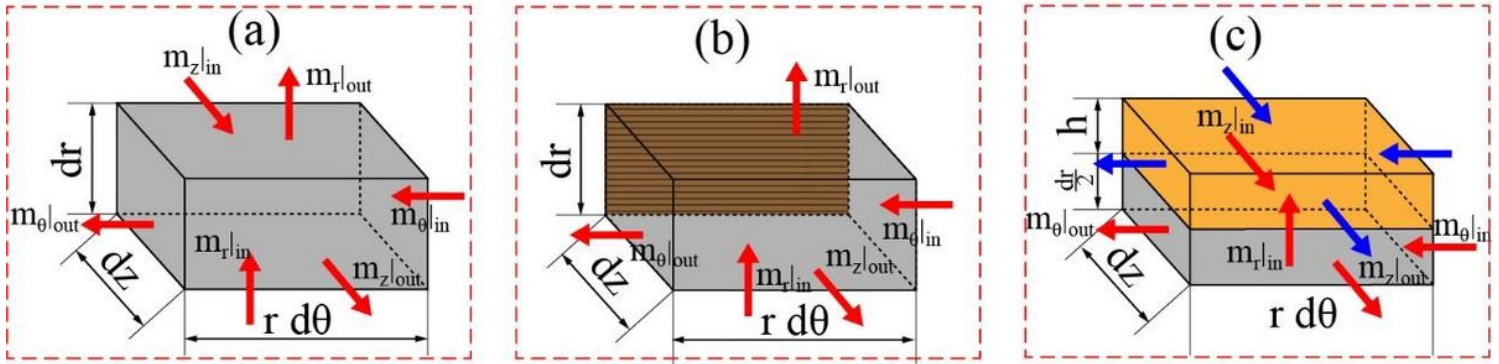


Figure 3

Airflow model in a PAJB

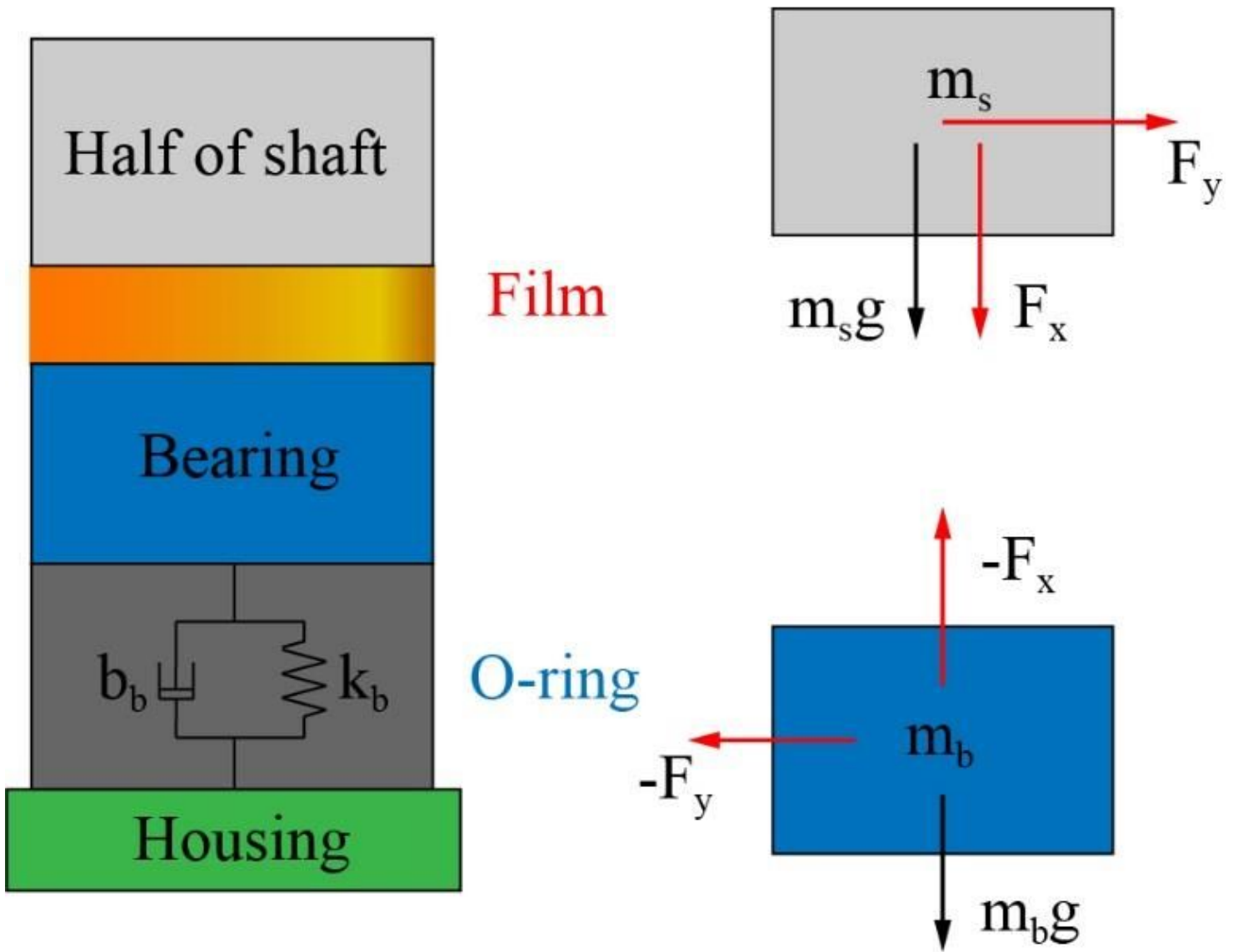


Figure 4

Mechanical model of the RPS

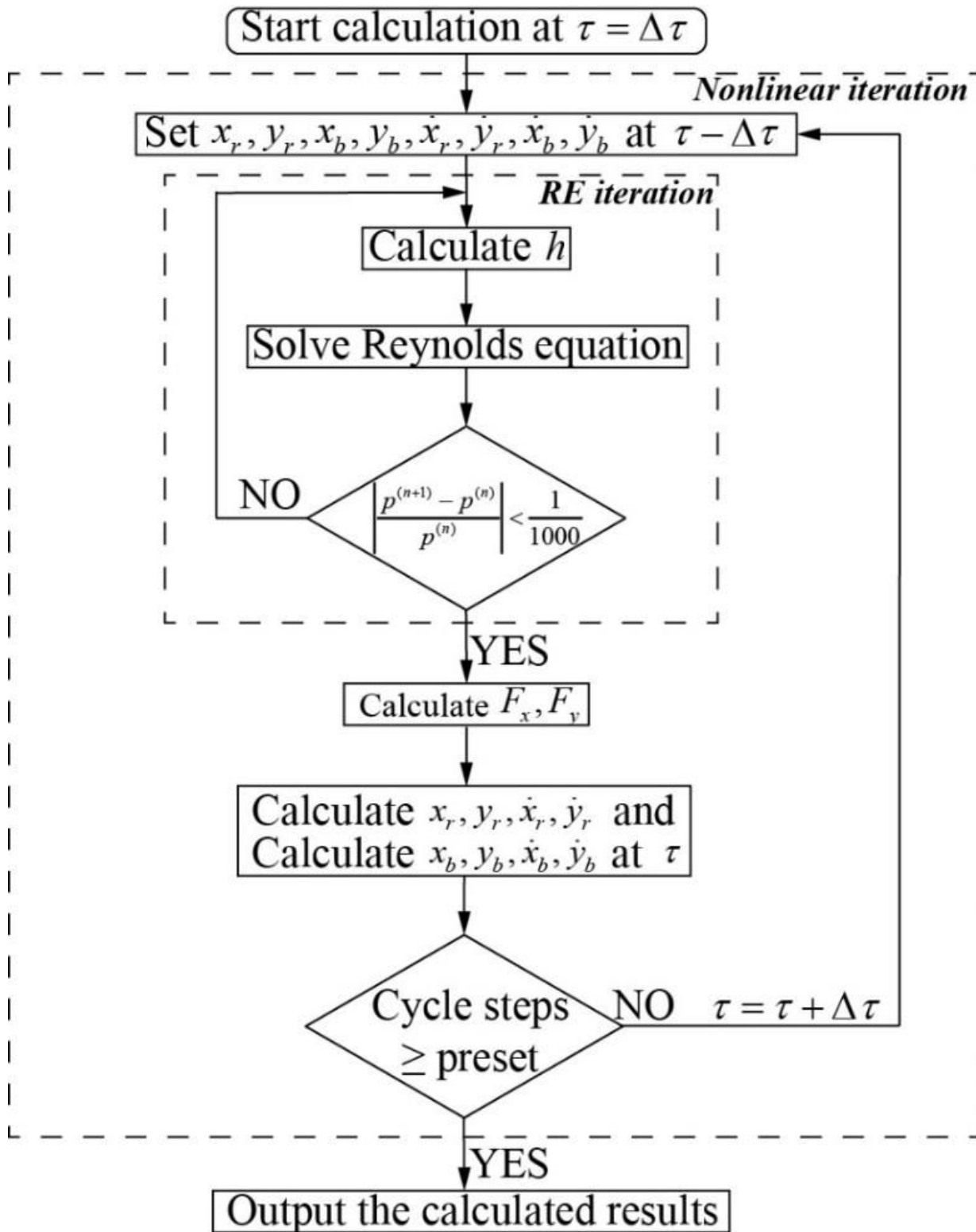


Figure 5

Flow chart of iteration method to obtain the characteristics of the RPS

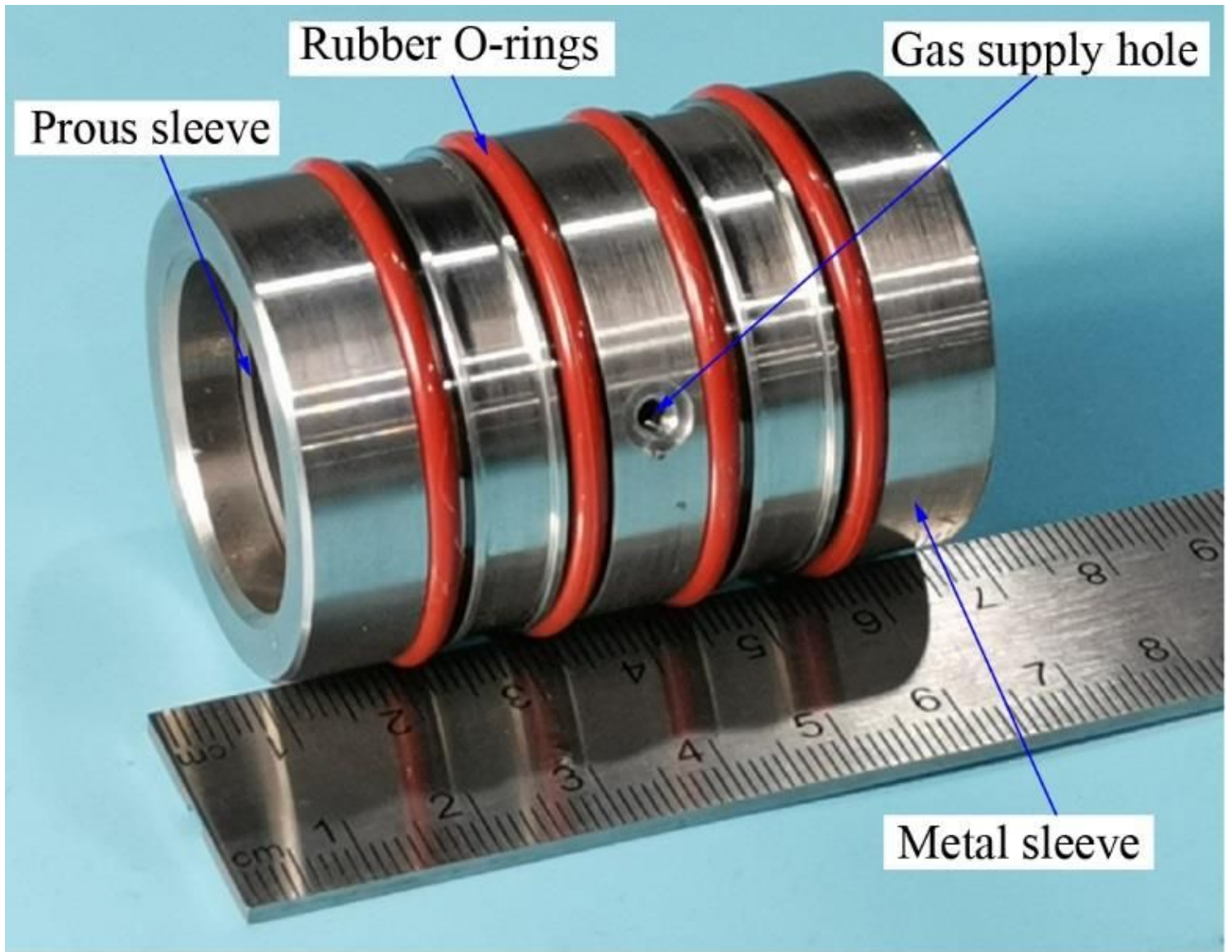


Figure 6

Photograph of the PAJB

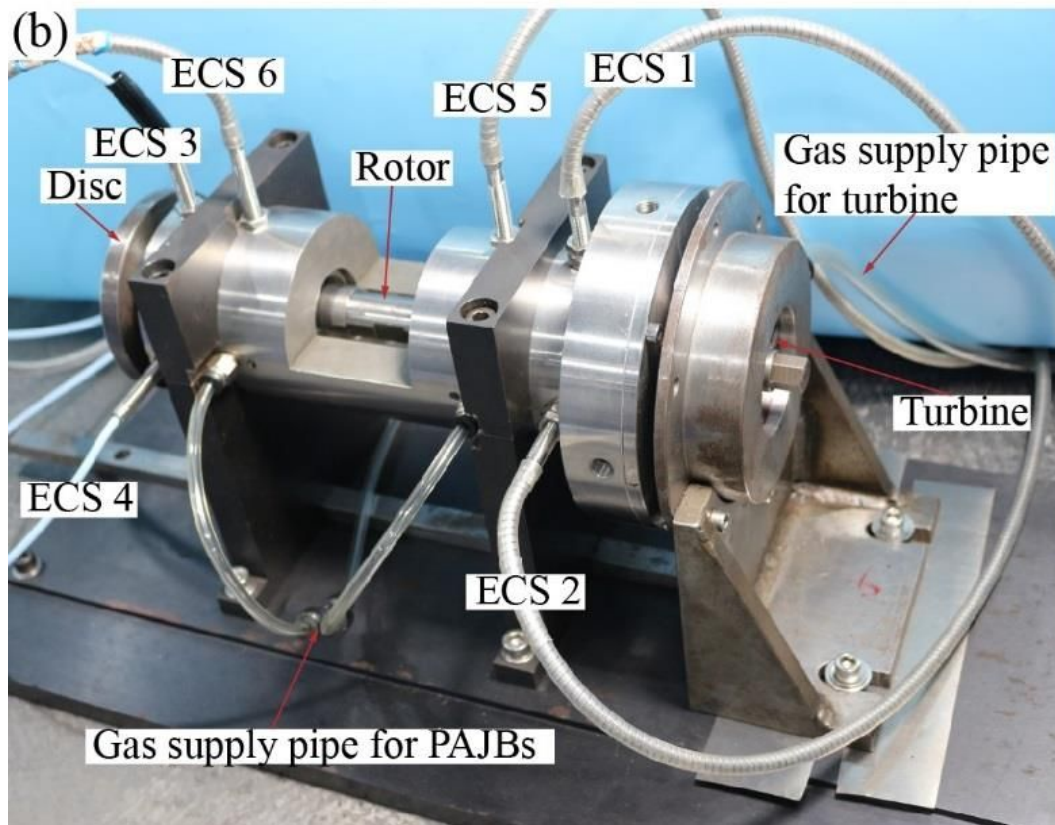
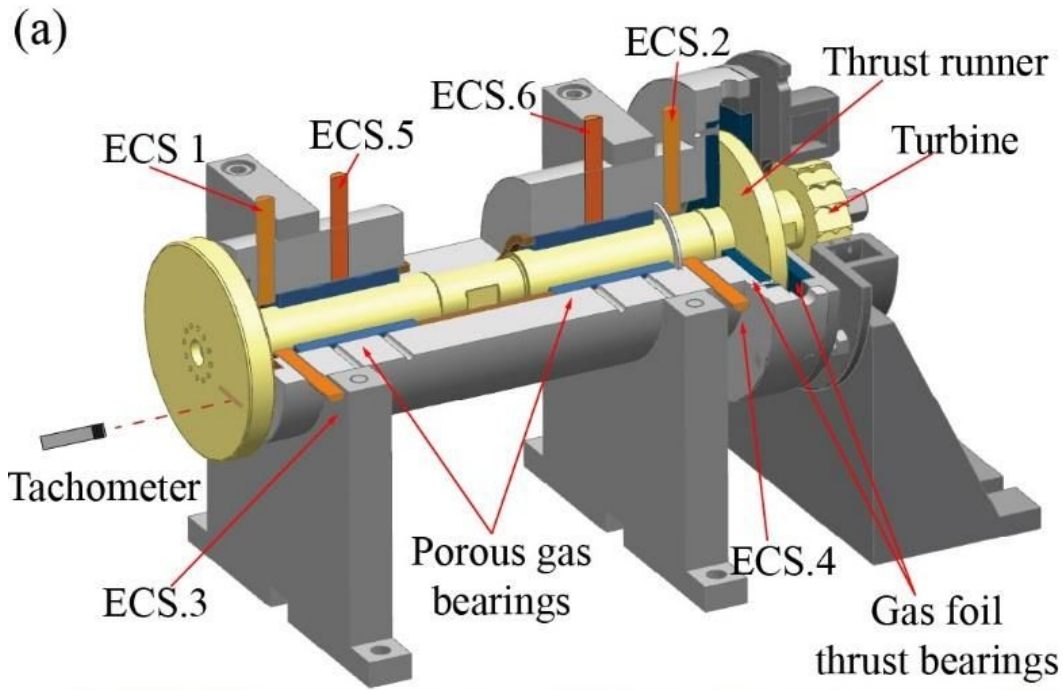
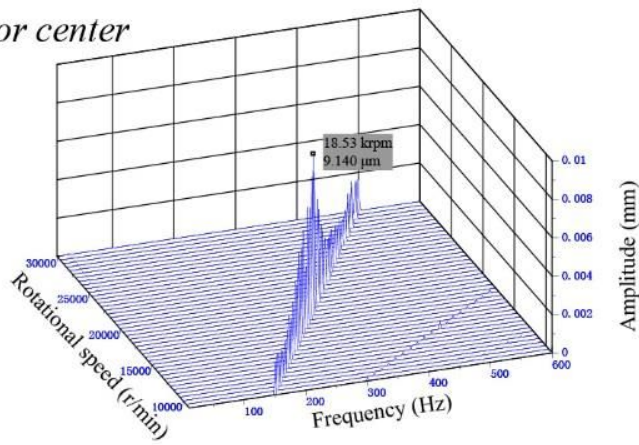


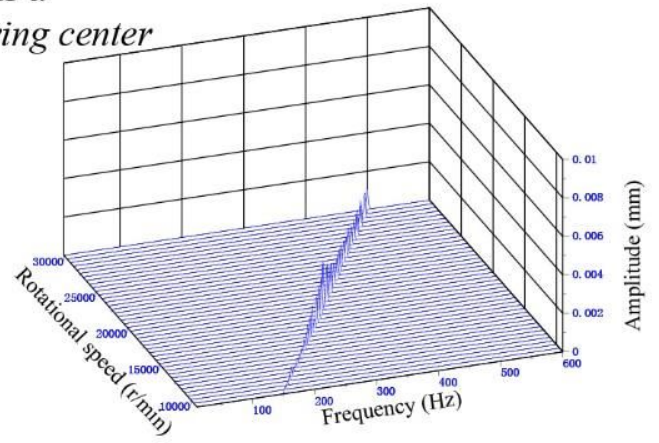
Figure 7

(a) Schematic diagram and (b) physical map of the rotor-bearing test-rig for RPS with O-rings mounted

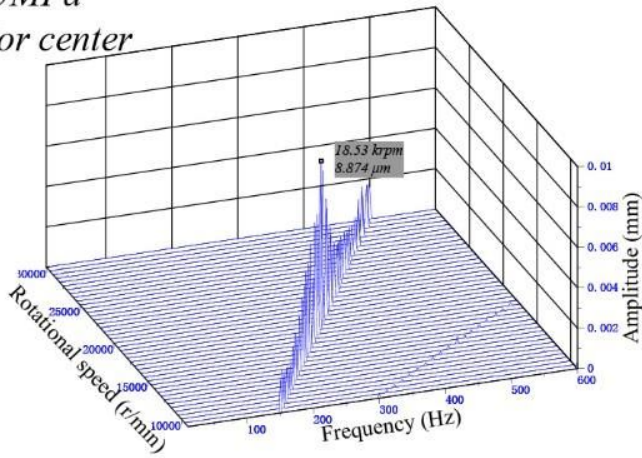
0.5MPa
Rotor center



0.5MPa
Bearing center



0.55MPa
Rotor center



0.55MPa
Bearing center

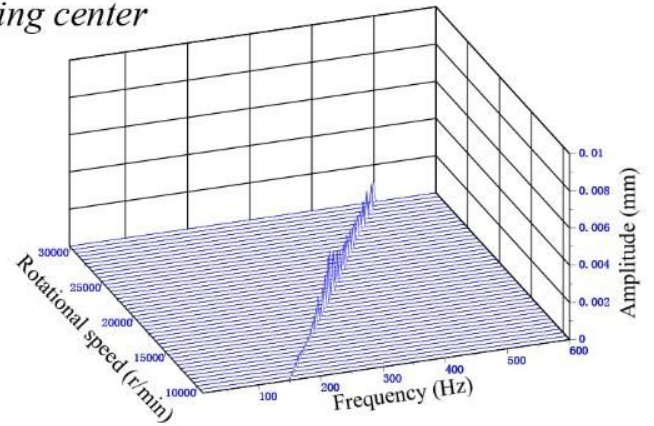


Figure 8

Waterfall plots (vertical direction) of the rotor and bearing centers for the RPS at the end of turbine

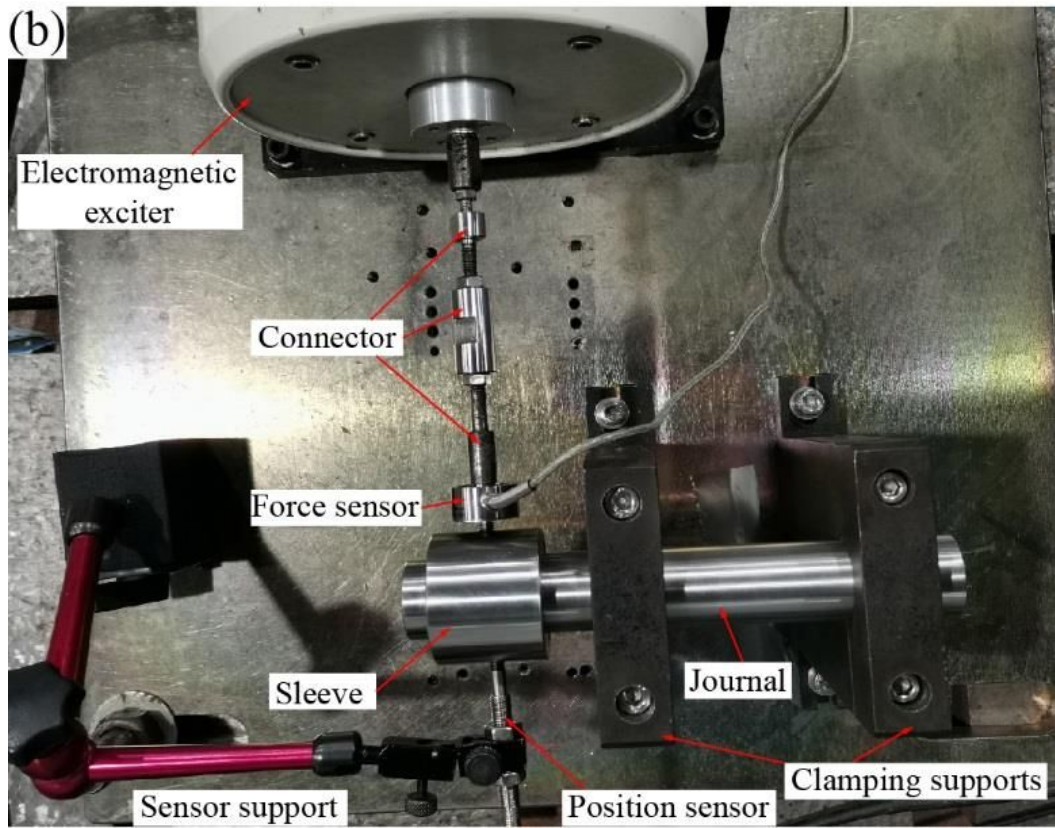
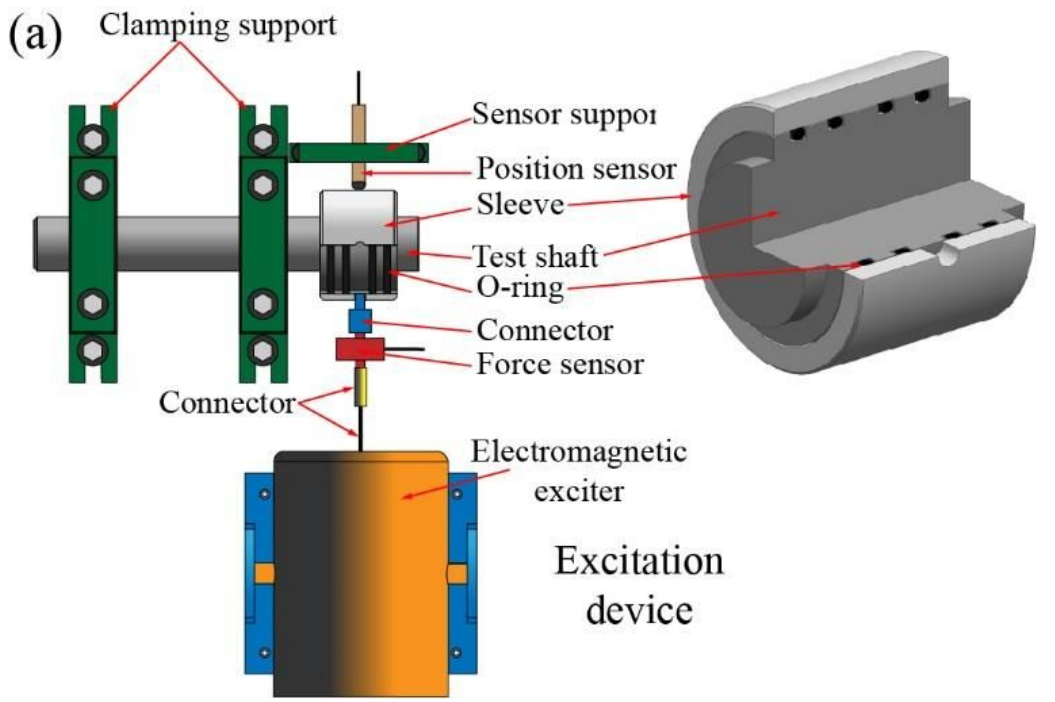


Figure 9

(a) Schematic diagram and (b) physical map of the excitation test-rig

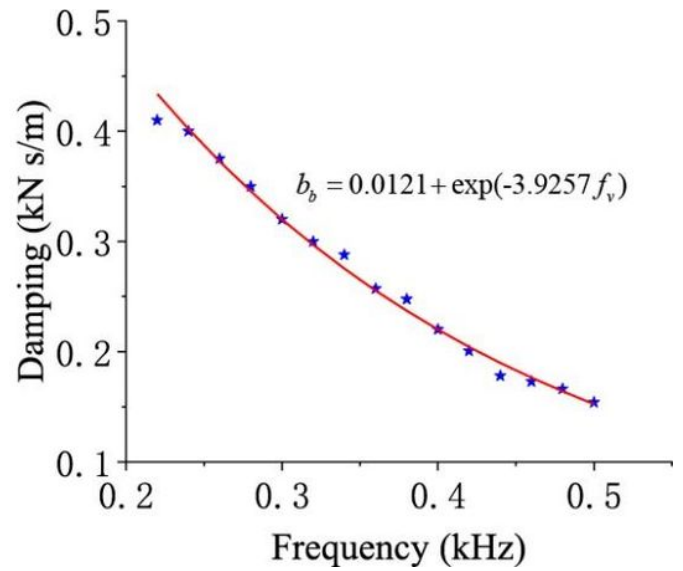
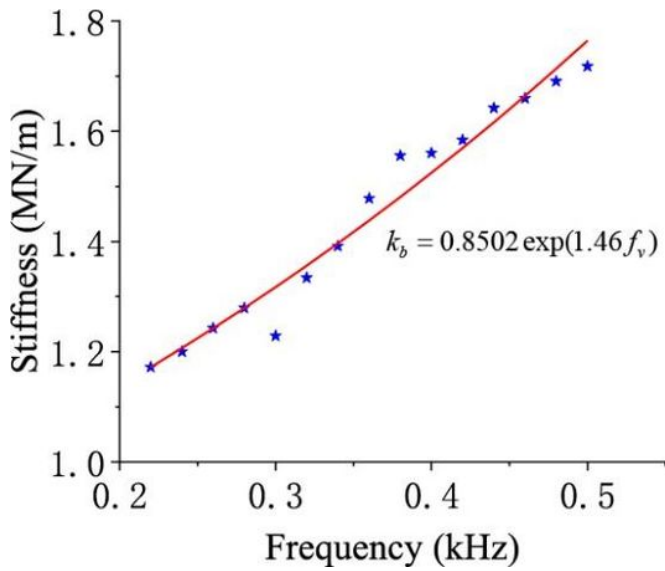


Figure 10

Stiffness and damping of an O-ring with the HNBR material varying with frequency

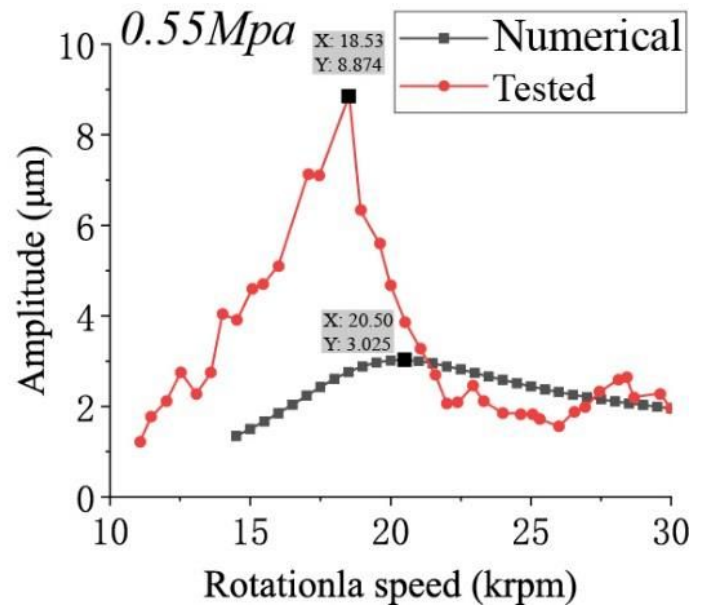
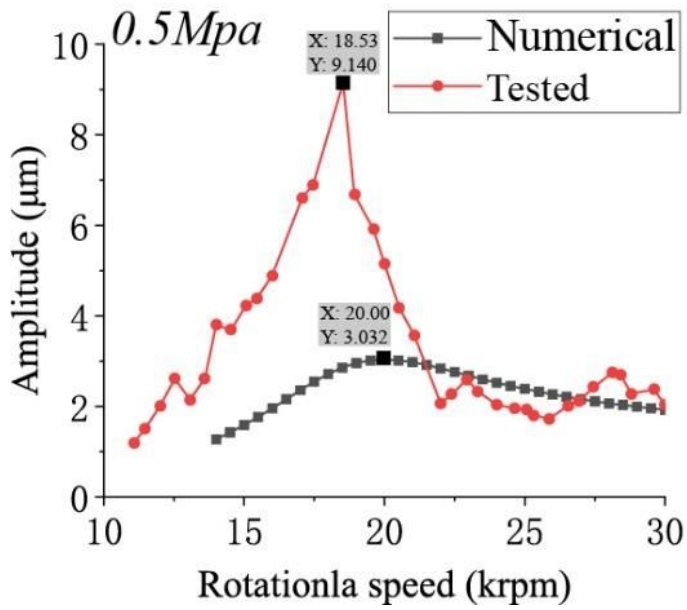


Figure 11

Comparison of the numerically calculated and experimentally tested synchronous amplitudes of the rotor in the vertical direction with a rotational speed of 12–30 krpm and external supply pressure values of 0.5 and 0.55 MPa

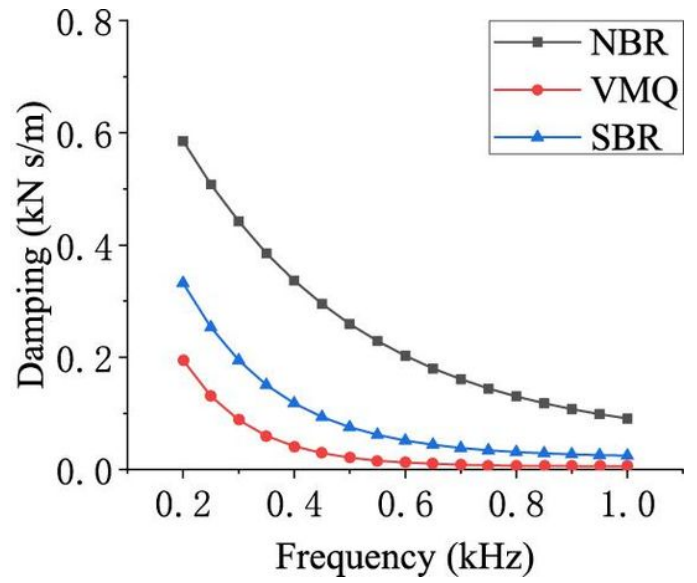
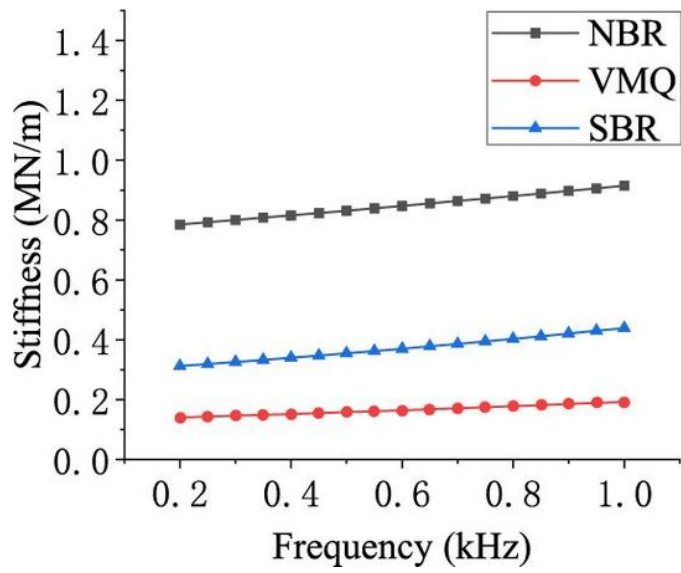


Figure 12

Empirical formulae for the three types of test O-rings in 0.2–1.0 kHz [27]

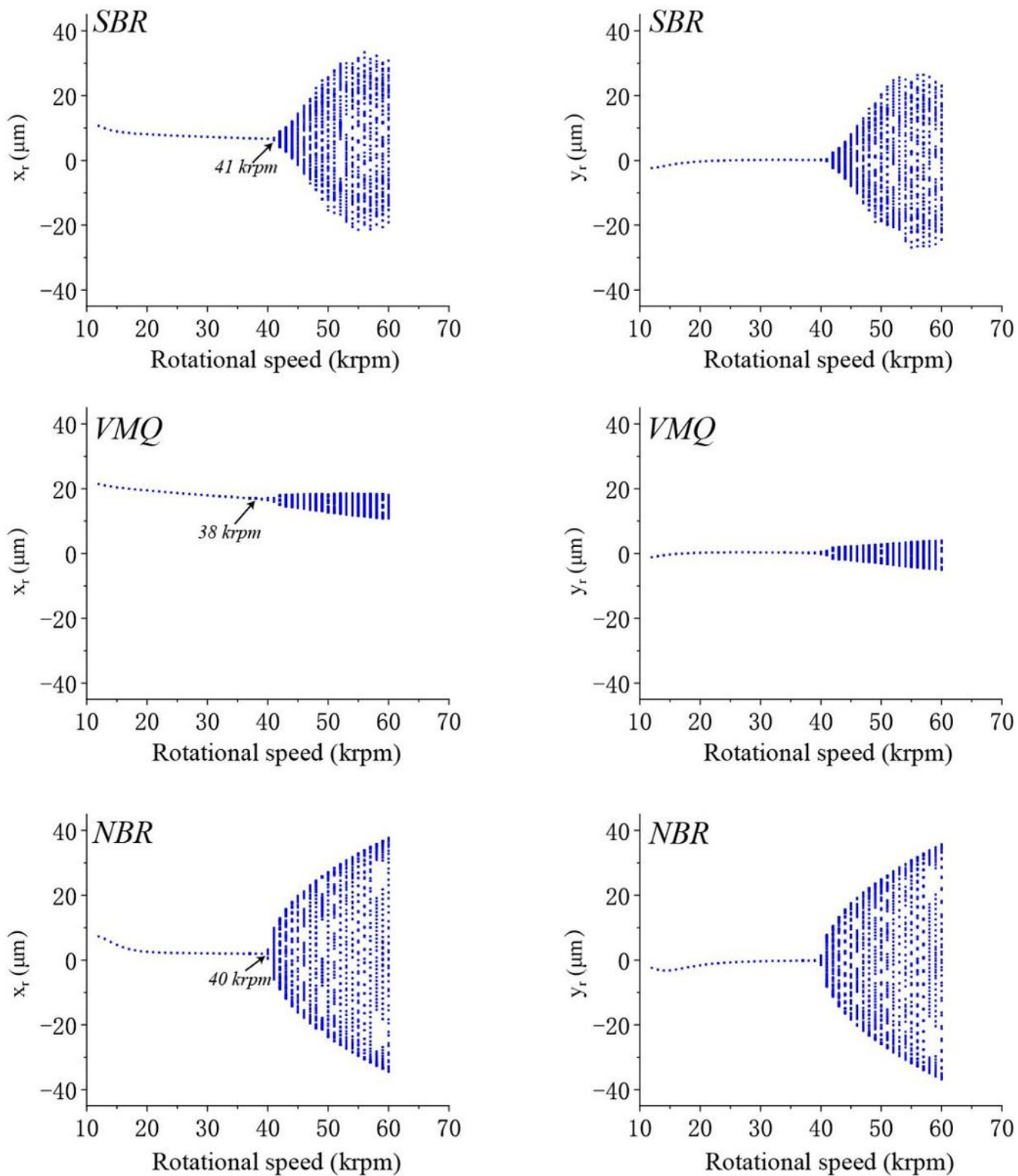


Figure 13

Bifurcation diagram of the absolute vibration of the rotor versus rotational speed (12–60 krpm) with rotor supported on BSBR, BVMQ, and BNBR

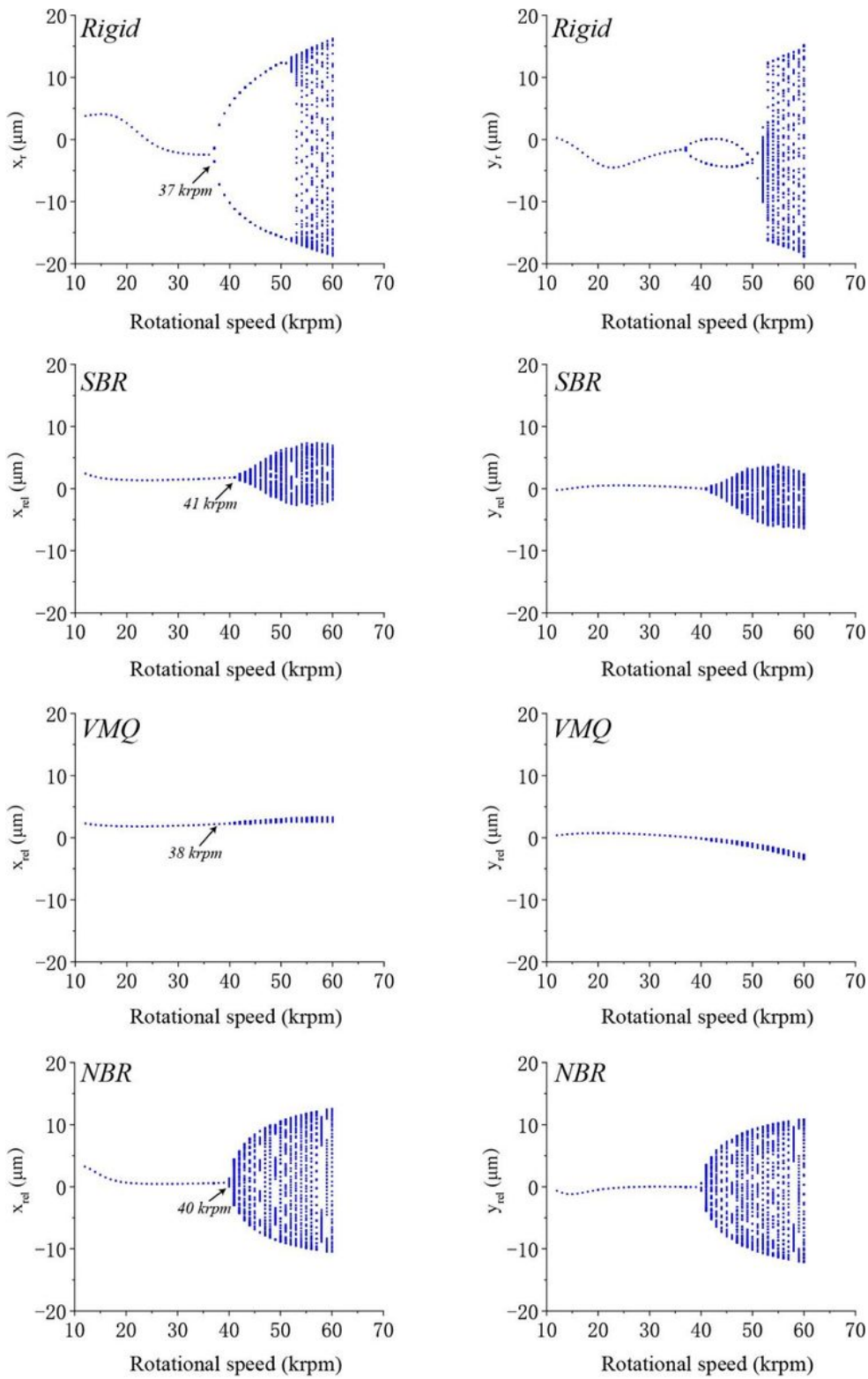


Figure 14

Bifurcation diagram of the relative vibration of the rotor versus rotational speed (12–60 krpm) when the rotor is supported on BR, BSBR, BVMQ, and BNBR

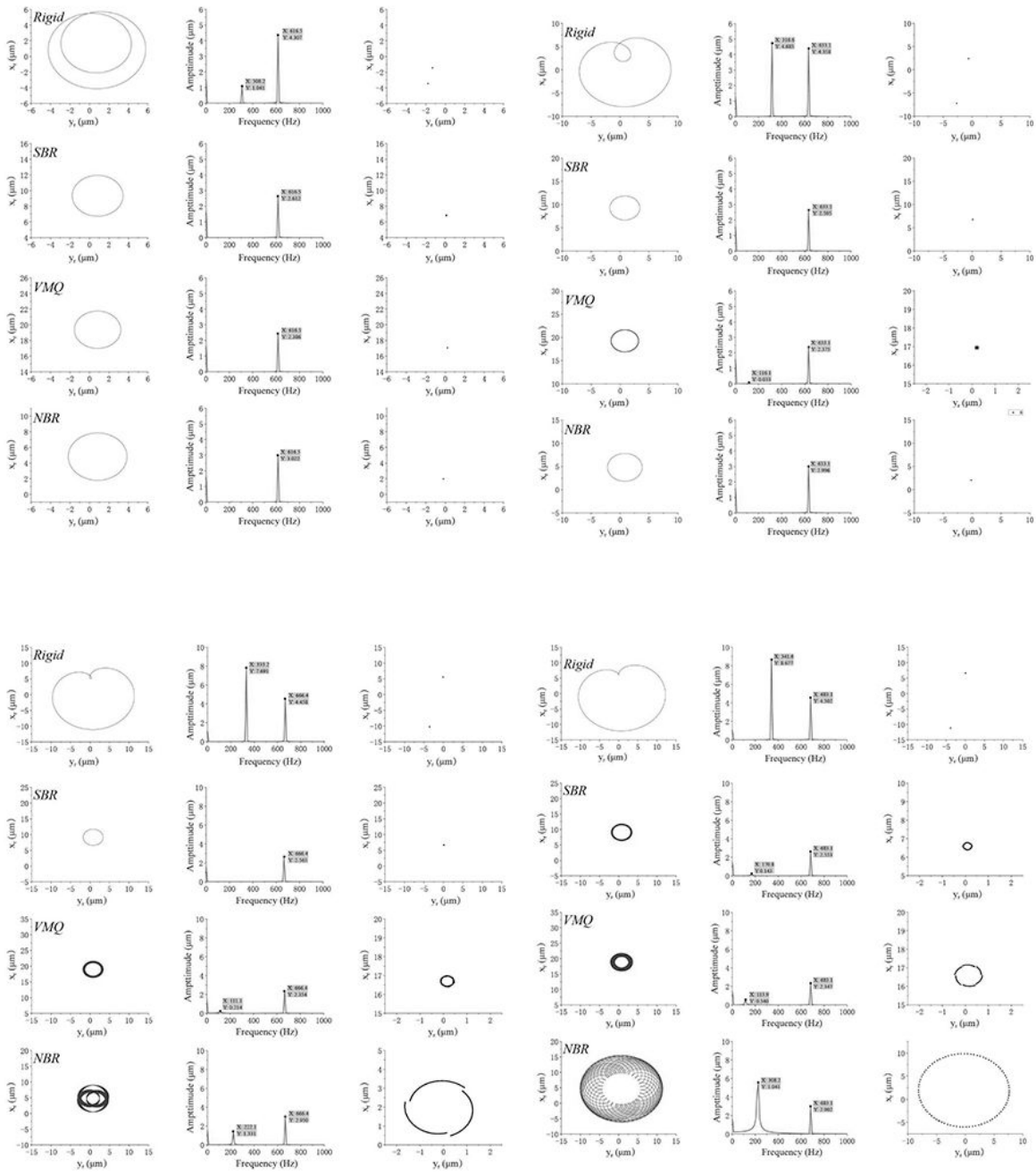


Figure 15

Predicted relative orbit and Poincaré maps of the rotor center and the FFT of the rotor center relative displacement in the horizontal direction with different rotational speeds: (a) 37, (b) 38, (c) 40, and (d) 41 krpm

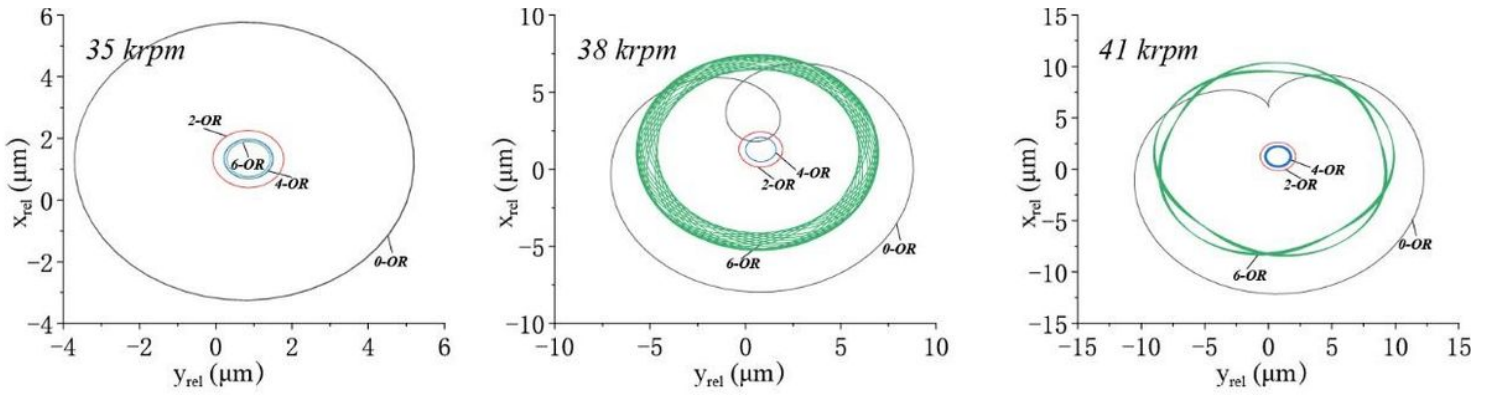


Figure 16

Predicted relative orbit of the rotor for the RPS with different numbers of SBRO mounted when the rotational speeds are 35, 38, and 41 krpm

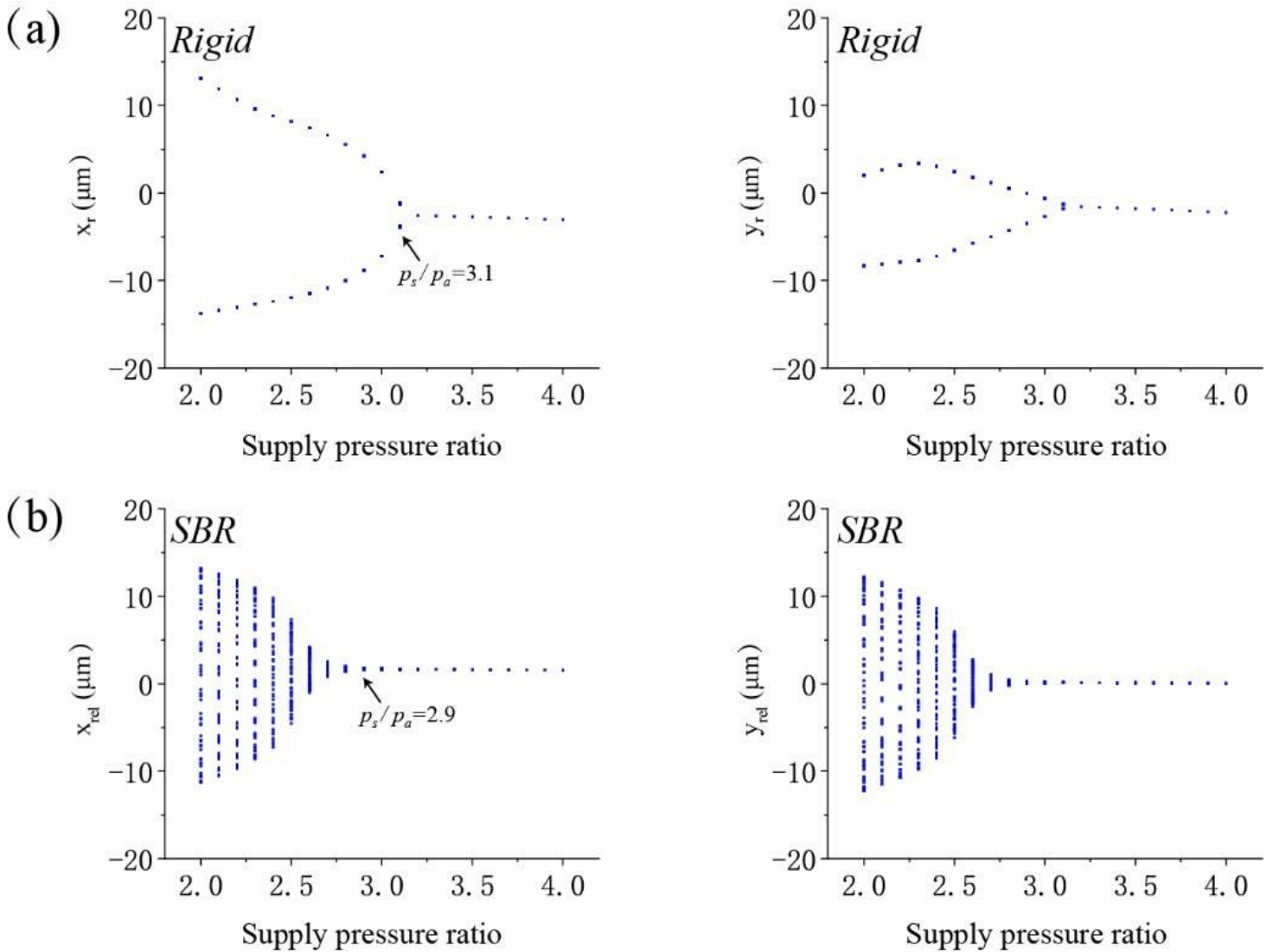


Figure 17

Bifurcation diagram of the relative vibration of the rotor versus external supply pressure (2–4 bar) when it is supported on (a) BR and (b) BSBR

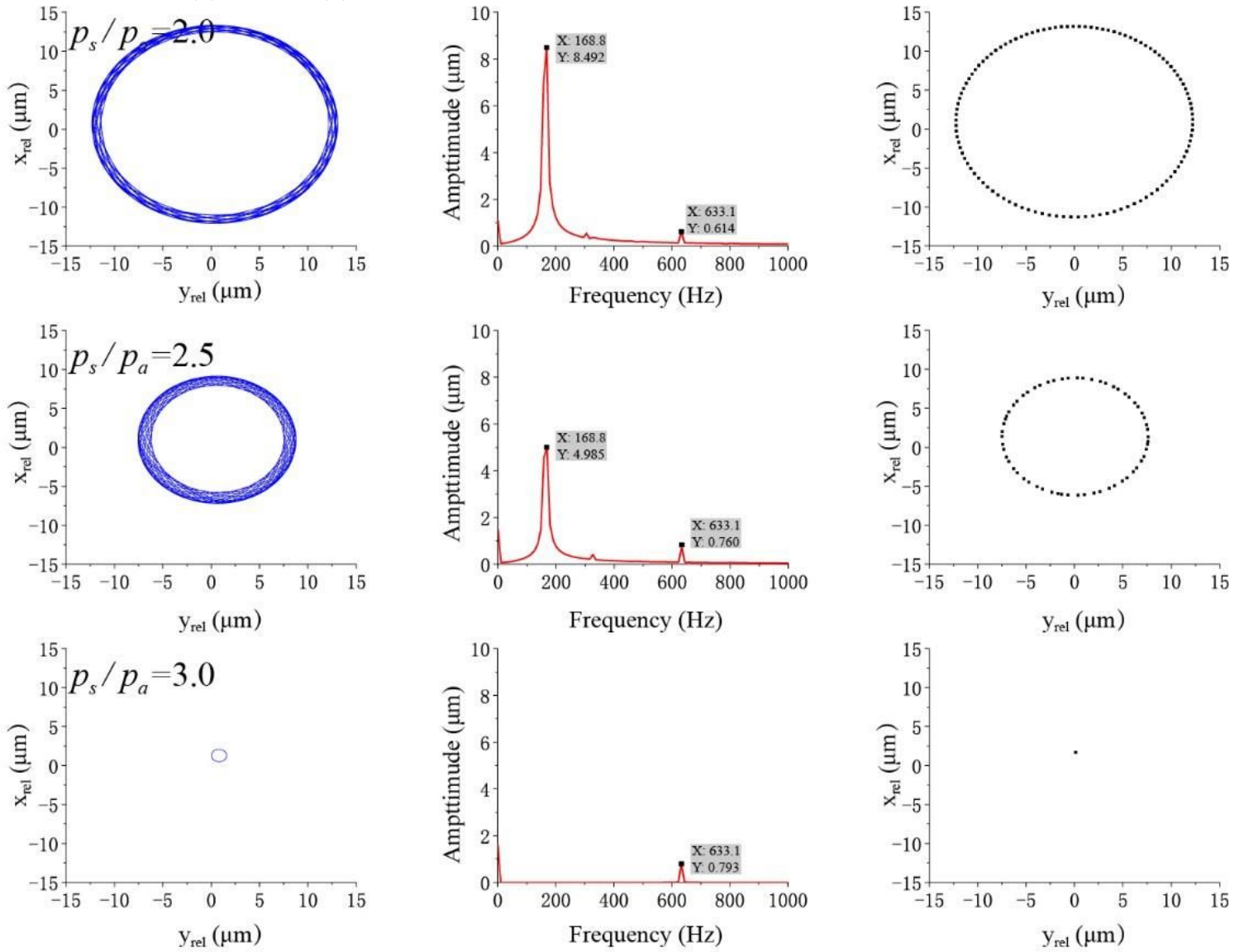


Figure 18

Predicted relative orbit and Poincaré maps of the rotor center and FFT of the rotor center relative displacement in the horizontal direction with different supply pressure values

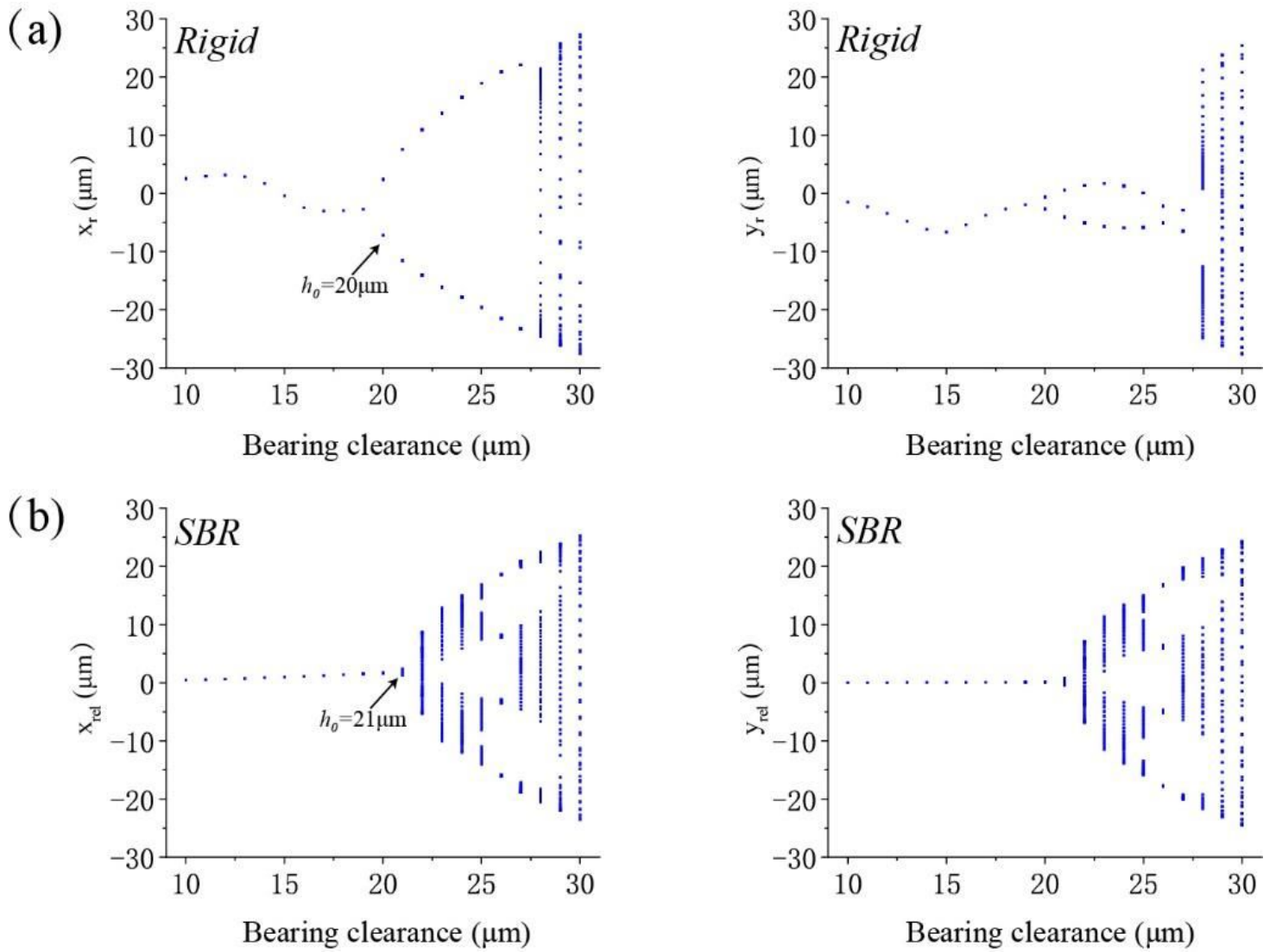


Figure 19

Bifurcation diagram of the relative vibration of the rotor versus the bearing clearance (10–30 μm) when it is supported on (a) BR and (b) BSBR

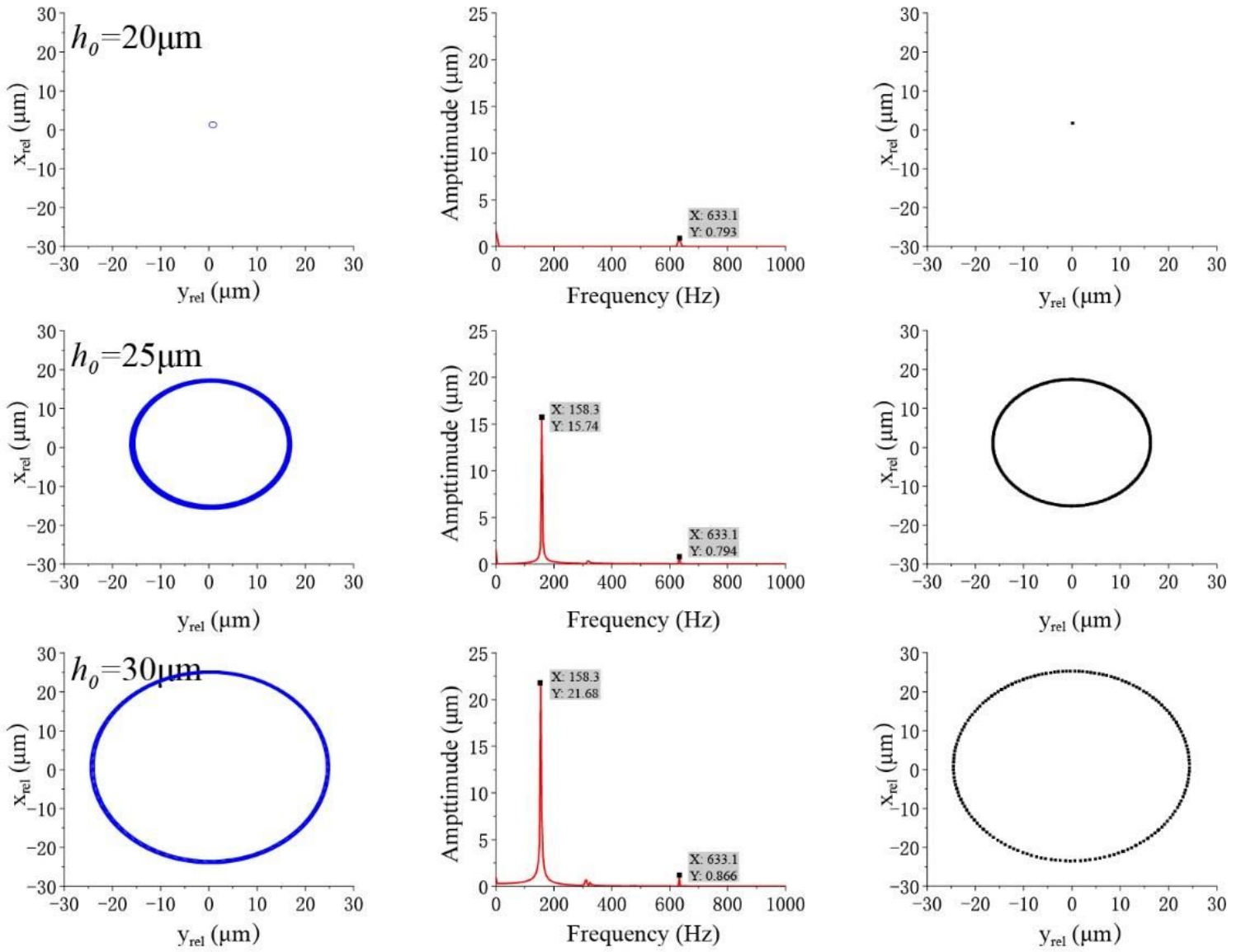


Figure 20

Predicted relative orbit and Poincaré map of the rotor center and the FFT of the rotor center relative displacement in the horizontal direction with different bearing clearances

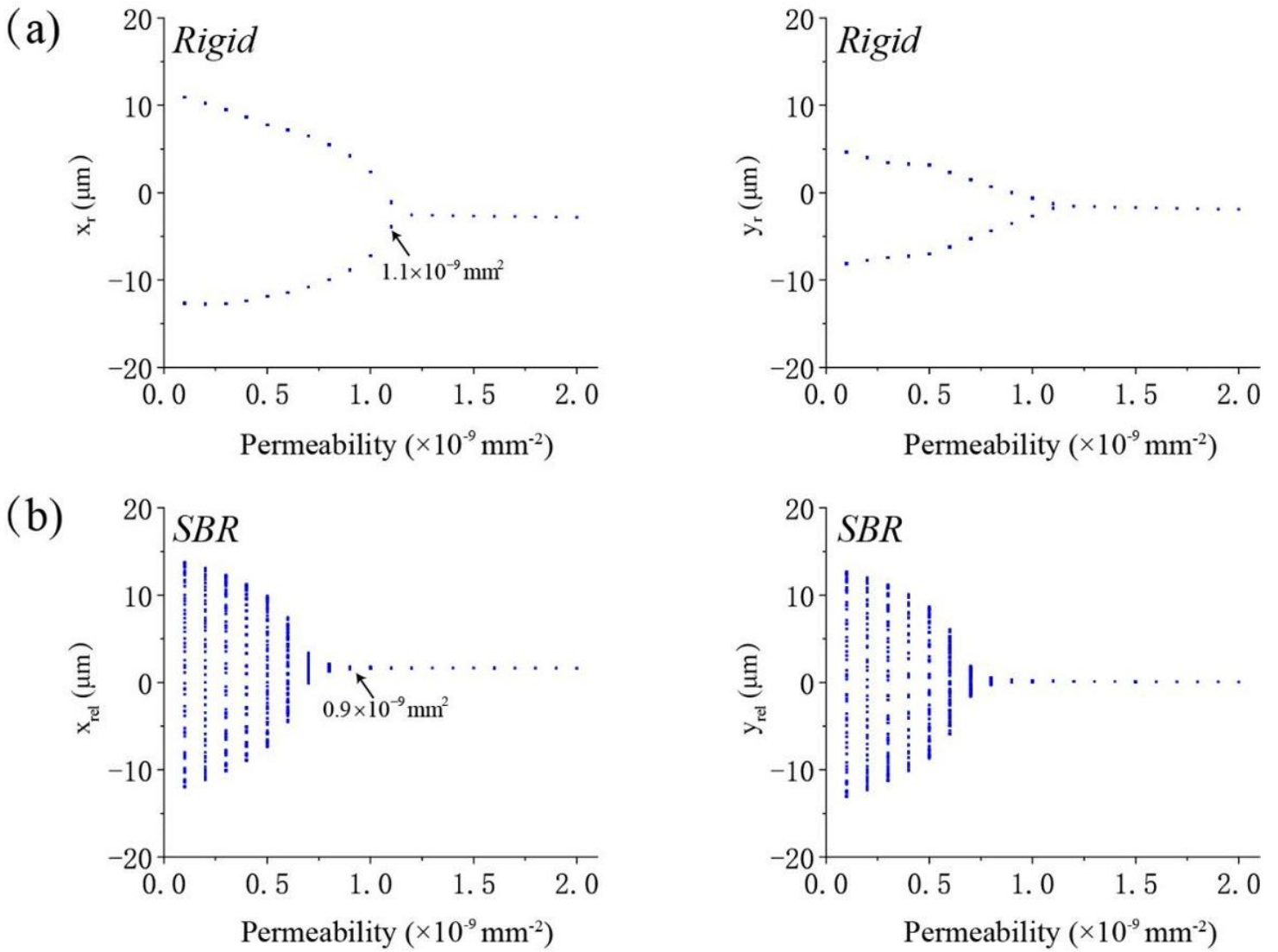


Figure 21

Bifurcation diagram of the relative vibration of the rotor versus porous permeability ($0.1 \times 10^{-9} - 2 \times 10^{-9} \text{ mm}^{-2}$) when it is supported on (a) BR and (b) BSBR.

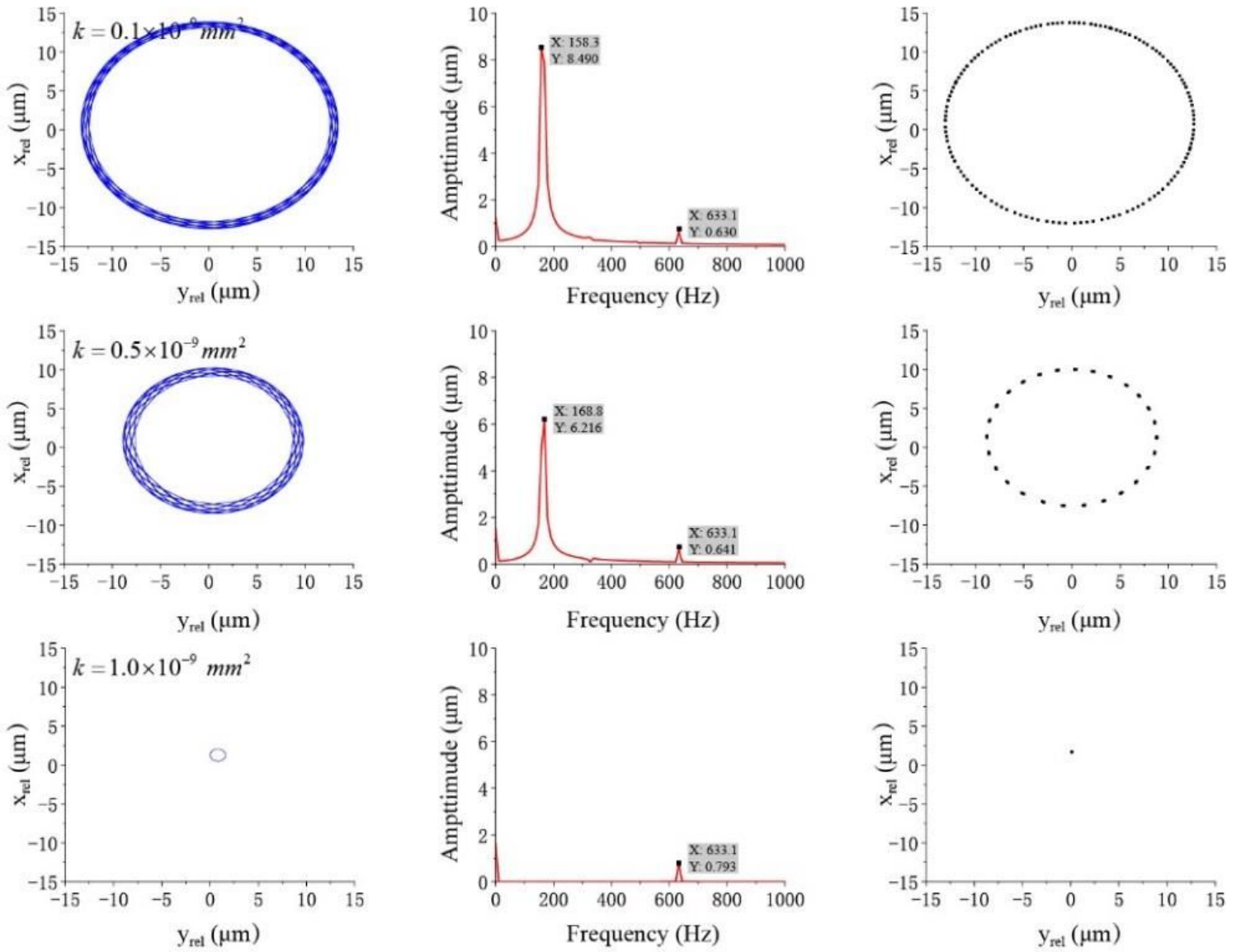


Figure 22

Predicted relative orbit and Poincaré map of the rotor center and the FFT of the rotor center relative displacement in the horizontal direction with different porous permeabilities